

学位論文 (要約)

Structures and dynamics  
of a MATE multidrug transporter from *Vibrio cholerae*  
(*Vibrio cholerae* に由来する多剤排出輸送体 MATE の  
構造とダイナミクス)

平成 28 年 12 月博士 (理学) 申請

東京大学大学院理学系研究科

生物科学専攻

草木迫 司



## Abstract

Exporting harmful substances from the intracellular environment to the extracellular milieu is one of the basic cellular defense systems. The efflux of toxic compounds or xenobiotics is accomplished by membrane proteins called “multidrug transporters”. Multidrug and toxic compound extrusion (MATE) family proteins are multidrug transporters conserved among bacteria, archaea, and eukaryotes. MATE transporters actively antiport xenobiotics, such as antibiotics and organic cations, using a  $\text{Na}^+$  or  $\text{H}^+$  ion gradient. Thus, MATE transporters confer multidrug resistance to pathogens. In the past few years, good progress has been made in the biochemical and structural studies of MATE transporters. All previously reported crystal structures of prokaryotic MATE transporters comprise 12 transmembrane (TM) helices, which are divided into the N- and C-lobes consisting of the TM1-TM6 and TM7-TM12 helices, respectively. Despite this structural knowledge, the molecular mechanism by which MATE transporters transport substrates coupled to the conformational change remains elusive. In this study, high-resolution crystal structures of a prokaryotic MATE homolog were determined, and a dynamics analysis was performed using double electron-electron resonance (DEER) spectroscopy.

One of the MATE transporters from *Vibrio cholerae*, VcmN, was chosen for the structural analysis. Purified VcmN was crystallized using the lipidic cubic phase (LCP) method. The crystal structures of VcmN in two distinct conformations (forms I and II) were determined at resolutions of 2.2 and 2.5 Å, respectively. As in the previously reported structures, the overall structure of VcmN is composed of the N- (TM1-TM6) and C-lobes (TM7-TM12). The central cleft formed between the N- and C-lobes is opened toward the extracellular side. Furthermore, a crevice laterally open to the membrane exists between TM2 in the N-lobe and TM7 in the C-lobe. Although the two structures are superimposed well, the TM1 helix adopts different conformations. The TM1 structure of form I is a typical straight helix. In contrast, the TM1 structure of form II is kinked at Pro20.

Thus, forms I and II were designated as the straight and bent forms, respectively. A similar conformational change of TM1 was observed in the previously solved structures of a MATE homolog from *Pyrococcus furiosus* (PfMATE). Therefore, the present observation revealed that the conformational change observed in the structures of archaeal H<sup>+</sup>-driven MATE transporters also occurs in the structures of bacterial H<sup>+</sup>-driven MATE transporters. In the C-terminal half of the TM1 helix, several amino acids, including Asp35, form a hydrogen-bonding network. Notably, the hydrogen-bonding network is rearranged between the straight and bent forms. The hydrogen-bonding patterns and geometries suggested that Asp 35 is deprotonated in the straight form and protonated in the bent form. These results implied that the H<sup>+</sup> binding to Asp35 and the rearrangement of the hydrogen-bonding network result in the protrusion of the C-terminal half of the TM1 helix, and thus the bending of the TM1 helix at Pro20. In the straight form, lipid monoolein molecules used in the LCP crystallization bind to the N-lobe cavity, and thus the monoolein molecules are likely to be mimicking the substrate of VcmN. Since the substrate binds to the N-lobe cavity in PfMATE, the N-lobe cavity of VcmN is also presumed to be the substrate-binding site. In the bent form of VcmN, the volume of the N-lobe shrinks by the conformational change of TM1. The previous studies of PfMATE suggested that the shrinking of the N-lobe cavity plays a role to inhibit the rebinding of substrates. Considering the similar conformational changes of VcmN and PfMATE, the substrate transport mechanism may also be conserved in VcmN.

To complement the pH-dependent TM1 conformational change, the dynamics analysis of VcmN was performed using double electron-electron resonance (DEER) spectroscopy. Two specific residues were replaced with Cys residues in a Cys-less background, based on the structural information. The electron spin label pairs were introduced into the Cys residues, and the distance distributions were measured under different pH conditions. The results revealed that the distance distributions of V34C/T263C (TM1/TM8) and V34C/H132C (TM1/TM4) were shifted to shorter

distance components under low pH conditions. Moreover, similar results were obtained not only in detergent but also in nanodisc lipid bilayer environments. These results supported the H<sup>+</sup>-dependent conformational change of TM1. Furthermore, to understand the dynamics during the entire transport cycle, the distance distributions of the extracellular and intracellular ends of TM were measured under different pH conditions. The results suggested that the intracellular side of VcmN is rigid, relative to the extracellular side.

Taken together, these results suggested that the rearrangement of the hydrogen-bonding network in the N-lobe and the conformational change of TM1 are common transport mechanisms conserved in the bacterial and archaeal H<sup>+</sup>-driven MATE transporters. Furthermore, in addition to the classical rocker-switch alternating access mechanism, in which transporters alternate between the outward-open and inward-open states, an alternative transport cycle was suggested. In the alternative transport cycle, which does not involve the inward-open conformation, the lipophilic substrates are probably transported directly from the lipid bilayer through the lateral crevice.

# Contents

Abstract.....	i
Contents .....	iv
Table of Abbreviations.....	vi
Table of Amino Acid Abbreviations.....	viii
Chapter 1 General Introduction .....	1
1.1 Membrane transporters .....	1
1.2 Multidrug transporters .....	3
1.3 Multidrug and toxic compound extrusion (MATE) family transporters .....	7
1.3.1 Discovery of MATE family transporters.....	7
1.3.2 MATE transporters from <i>Vibrio cholerae</i> .....	8
1.3.3 Structures and functions of MATE transporters.....	8
1.3.4 Two distinct transport models by H <sup>+</sup> -driven prokaryotic MATE transporters .....	9
1.3.5 Dynamics and molecular mechanism of MATE transporters.....	10
1.4 Overview of this study.....	11
Figures and Tables of Chapter 1 .....	12
Figure 1-1 Schematic diagram of membrane transport proteins.....	12
Figure 1-2 Known multidrug transporters .....	13
Figure 1-3 Phylogenetic tree of prokaryotic MATE transporters.....	14
Figure 1-4 Representative substrates of MATE transporters .....	15
Figure 1-5 Previously reported structures of MATE transporters.....	16
Figure 1-6 Distinct transport models of prokaryotic H <sup>+</sup> -driven transporters .....	17
Table 1-1 MICs of various drugs in <i>E. coli</i> KAM32 harboring plasmid carrying each MATE gene from <i>Vibrio cholerae</i> .....	18
Table 1-2 Previously reported structures of MATE transporters.....	19
Chapter 2 X-ray crystallographic analysis of VcmN, a MATE multidrug transporter from <i>Vibrio cholerae</i> .....	20
2.1 Introduction.....	20
2.2 Materials and Methods.....	20
2.2.1 Plasmid construction.....	20
2.2.2 Expression and purification of VcmN.....	21
2.2.3 Crystallization of VcmN .....	23
2.2.4 X-ray diffraction analysis and data processing .....	24

2.2.5 Model building and structure refinement.....	26
2.3 Results and Discussion .....	26
2.3.1 Expression, purification and construct optimization of VcmN.....	26
2.3.2 Crystallization of VcmN .....	27
2.3.3 X-ray diffraction analysis.....	28
2.3.4 Phase determination, model building and structure refinement.....	29
Figures and Tables of Chapter 2 .....	30
Figure 2-1 Schematic diagram of the VcmN crystallization construct .....	30
Figure 2-2 Size-exclusion chromatograms and SDS-PAGE analysis .....	31
Figure 2-3 Crystals of VcmN $\Delta$ C.....	32
Figure 2-4 X-ray diffraction images .....	33
Figure 2-5 Matthew's coefficient.....	34
Figure 2-6 Electron density map (Form I) .....	35
Figure 2-7 Electron density map (Form II).....	36
Figure 2-8 Ramachandran plots .....	37
Figure 2-9 Crystal packing.....	38
Table 2-1 Macromolecule-production information .....	39
Table 2-2 DNA primers for construct optimization .....	40
Table 2-3 Buffer composition .....	40
Table 2-4 Crystallization conditions .....	41
Table 2-5 Data collection statistics .....	42
Table 2-6 Refinement statistics .....	43
Chapter 3 Crystal structures of VcmN.....	44
Chapter 4 Dynamics analysis of VcmN using DEER spectroscopy .....	45
Chapter 5 General Discussion.....	46
References.....	47
Original papers.....	54
Acknowledgements.....	55

## Table of Abbreviations

Abbreviation	Full name
ABC	ATP-binding cassette
APBS	adaptive Poisson-Boltzmann solver
ATP	adenosine triphosphate
CBB	coomassie brilliant blue
CCD	charge coupled device
CFLX	ciprofloxacin
CM	chloramphenicol
DDM	n-Dodecyl $\beta$ -D-maltopyranoside
DEER	double electron-electron resonance
DinF	DNA damage-inducible protein F
DME	dimethyl ether
DMT	drug/metabolite transporter
DNA	deoxyribonucleic acid
DTT	dithiothreitol
EC	evolutionary constraint
EDTA	ethylenediaminetetraacetic acid
EPR	electron paramagnetic resonance
EtBr	ethidium bromide
Hoech	Hoechst 33342
IPTG	isopropyl $\beta$ -D-thiogalactopyranoside
KM	kanamycin
LB	Luria-Bertani
LCP	lipidic cubic phase
MATE	multidrug and toxic compound extrusion
MD	molecular dynamics
MDR	multidrug resistance
MES	2-morpholinoethanesulfonic acid

MFS	major facilitator superfamily
MO	monoolein
MSP	membrane scaffold protein
MTSSL	1-oxy-2,2,5,5-tetramethylpyrroline-3-methyl methanethiosulfonate
MWCO	molecular weight cutoff
NBD	nucleotide-binding domain
NFLX	norfloxacin
Ni-NTA	nickel-nitrilotriacetic acid
NMR	nuclear magnetic resonance
OFLX	ofloxacin
PACE	proteobacterial antimicrobial compound efflux
PCR	polymerase chain reaction
PDB	Protein Data Bank
PEG	polyethylene glycol
PMSF	phenylmethylsulfonyl fluoride
POPC	1-palmitoyl-2-oleoyl-sn-glycero-3-phosphocholine
RND	resistance-nodulation-cell division
SDS-PAGE	sodium dodecyl sulfate poly-acrylamide gel electrophoresis
SEC	size-exclusion chromatography
SM	streptomycin
SMR	small multidrug resistance
TB	terrific broth
TEV	tobacco etch virus
TM	transmembrane
Tris	tris(hydroxymethyl)aminomethane
WT	wild type

---

Table of Amino Acid Abbreviations

Abbreviation	Full name
A, Ala	alanine
C, Cys	cysteine
D, Asp	aspartic acid
E, Glu	glutamic acid
F, Phe	phenylalanine
G, Gly	glycine
H, His	histidine
I, Ile	isoleucine
K, Lys	lysine
L, Leu	leucine
M, Met	methionine
N, Asn	asparagine
P, Pro	proline
Q, Gln	glutamine
R, Arg	arginine
S, Ser	serine
T, Thr	threonine
V, Val	valine
W, Trp	tryptophan
Y, Tyr	tyrosine

# Chapter 1 General Introduction

## 1.1 Membrane transporters

Cells, the basic units composing all living things, are separated from the external environment by the biological membrane. The biological membrane is mainly composed of phospholipids, which have hydrophobic regions consisting of acyl chains and hydrophilic regions consisting of a phosphate group. To maintain cellular viability, the cell must properly transport various molecules, such as ions, amino acids, sugars, nucleotides, and drugs, across the cell membrane. The transport of substances across the cell membrane is accomplished by membrane transport proteins. Membrane transport is classified into passive transport and active transport (**Figure 1-1a**). Passive transport is substrate transport in accordance with the electrochemical gradient. The membrane proteins contributing to passive transport are mainly ion channels. In contrast, active transport is substrate transport against the electrochemical gradient. The membrane transport proteins contributing to active transport are classified into the primary active transporters and the secondary active transporters, based on the driving force. The primary active transporters transport substrates using the energy obtained from ATP hydrolysis or light absorption. In contrast, the secondary active transporters transport substrates using the electrochemical gradient of ions produced by the primary active

transporters. The secondary active transporters are further classified into symporters and antiporters, based on the difference in the direction of the ion transport coupled to the substrate transport (**Figure 1-1b**). The symporters transport substrates in the same direction as the coupled ion flux. In contrast, the antiporters transport substrates in the opposite direction of the coupled ion flux. The secondary active transporters are considered to transport substrates by the alternating access mechanism (**Figure 1-1c**) (Jardetzky, 1966). The alternating access mechanism is classified into three different models, including rocker-switch, rocking-bundle, and elevator models (Shi, 2013; Drew and Boudker, 2016). Representative transporters for the rocker-switch alternating access mechanism are typically composed of two structurally similar bundles related by pseudo two-fold symmetry. The substrate-binding site is formed between the two bundles. During the transport cycle, rocker-switch proteins adopt different conformations involving the outward-open, occluded, and inward-open states (**Figure 1-1c**). As a result, the substrate-binding site is exposed to the extracellular side and the intracellular side via distinct states. In addition to the global conformational change, the local rearrangements of the transmembrane (TM) helices occur during the substrate transport (Solcan et al., 2012; Deng et al., 2015; Fukuda et al., 2015).

## 1.2 Multidrug transporters

Exporting harmful substances from the intracellular environment to the extracellular milieu is one of the basic cellular defense systems. Among membrane transporters, those effluxing a broad range of harmful compounds are called multidrug transporters (**Figure 1-2**). Due to the efflux of multiple drugs, pathogens acquire multidrug resistance. The increase in multidrug-resistant pathogens that are difficult to treat using conventional antibiotics has become a global public health problem. To date, the multidrug transporters are classified into at least five families, including the ATP-binding cassette (ABC) superfamily, the resistance-nodulation-cell division (RND) family, the major facilitator superfamily (MFS), the small multidrug resistance (SMR) family, and the multidrug and toxic compound extrusion (MATE) family. In this section, the functional and structural characteristics of multidrug transporters, except for the MATE family proteins, are described as follows.

### (1) ABC superfamily transporters

The ABC transporters are “primary active transporters”, which transport substrates driven by the free energy of ATP binding and/or hydrolysis (Rees et al., 2009). The ABC transporters are widely distributed in the three domains of life. Well-known ABC superfamily multidrug transporters are ABCB1 (also known as MDR1 or P-

glycoprotein) (Chen et al., 1986; Aller et al., 2009; Jin et al., 2012) and its bacterial homolog Sav1866 (Dawson and Locher, 2006). The ABC transporters comprise the membrane domain dimer and the intracellular nucleotide-binding domain (NBD) dimer (Dawson and Locher, 2006; Perez et al., 2015; Locher, 2016). The subunits consisting of the membrane domain and the NBD domain are encoded either separately or as a single polypeptide. ATP binding induces the dimerization of the NBD, and ATP hydrolysis induces the dissociation of the NBD dimer. The conformational change of the NBD causes the conformational change of the transmembrane domain, resulting in the coupling to the substrate transport. The structures of the outward-facing and inward-facing states were reported (Dawson and Locher, 2006; Aller et al., 2009; Jin et al., 2012). Thus, ABC transporters are considered to transport substrates via the alternating access mechanism. The conformational change was investigated by a spectroscopic analysis (Mishra et al., 2014). Although the structures of both the outward-open and inward-open states have been reported, the ABC superfamily flippase PglK is considered to require only the outward-facing state for the flipping of the substrate lipid (Perez et al., 2015).

The following multidrug transporters are “secondary active transporters”, which transport substrates coupled to the electrochemical potential across the membrane.

## (2) RND family transporters

A well-studied representative of the RND family multidrug transporter is *E. coli* AcrB. AcrB recognizes a broad range of substrates, such as tetracycline, chloramphenicol,  $\beta$ -lactams, fusidic acids, and fluoroquinolones (Nishino et al., 2009). AcrB forms a homotrimer (Murakami et al., 2006). Each protomer of AcrB consists of a 12-helix transmembrane domain and a periplasmic portion composed of porter and funnel domains. The porter domain is divided into four subdomains, which form the two substrate-binding sites. One of the proposed transport pathways for substrates is through the outer leaflet of the membrane, via a TM8/TM9 groove entrance as a lateral pathway. During the substrate transport coupled to the proton translocation, the AcrB trimer cycles via three conformational states with distinct substrate-binding site shapes.

### (3) MFS transporters

The major facilitator superfamily (MFS) transporters are highly conserved among all domains of life (Yan, 2015). Typical structures of MFS transporters consist of 12 transmembrane (TM) helices. The TM helices are divided into the N- and C-bundles, each consisting of six TM helices. The N- and C-bundles are related by pseudo two-fold symmetry. A well-studied representative MFS multidrug transporter is *E. coli* EmrD (Yin et al., 2006). EmrD is considered to transport substrates via a rocker-switch alternating access mechanism, as described above. The proposed transport model was supported by

the spectroscopic analysis of LmrP (Masureel et al., 2014; Martens et al., 2016), an MFS multidrug transporter with an as yet undetermined structure.

#### (4) SMR family transporters

The SMR transporters are conserved in bacteria (Bay et al., 2008) and belong to the drug/metabolite transporter (DMT) superfamily. A well-studied representative SMR transporter is *E. coli* EmrE. Each protomer of EmrE comprises four TM helices inserted with a dual topology, forming antiparallel homodimers (Rapp and Granseth, 2007; Nara et al., 2007; Chen et al., 2007; Nasie et al., 2010). An alternating access mechanism of EmrE has been proposed, based on the outward-open and inward-open state structures (Korkhov and Tate, 2008; Morrison et al., 2011). The alternating access model was also investigated by a spectroscopic analysis (Dastvan et al., 2015).

In addition to the above four families, the proteobacterial antimicrobial compound efflux (PACE) family proteins have recently been characterized as multidrug transporters (Hassan et al., 2013; Hassan et al., 2015). More information about the PACE family transporters awaits further experimental exploration.

## 1.3 Multidrug and toxic compound extrusion (MATE) family transporters

### 1.3.1 Discovery of MATE family transporters

The MATE family proteins are highly conserved among bacteria, archaea, and eukaryotes, and are classified into three branches: the NorM, DNA damage-inducible protein F (DinF), and eukaryotic subfamilies (Omote et al., 2006). In 1998, a NorM gene was first cloned from the slightly halophilic marine bacterium *Vibrio parahaemolyticus* (Morita et al., 1998). Initially, NorM was suggested to be a member of the MFS transporters. However, due to its low sequence similarity with MFS transporters, NorM was newly annotated as a MATE family transporter (Brown et al., 1999). Further characterization revealed that *V. parahaemolyticus* NorM is a Na<sup>+</sup>-driven multidrug transporter (Morita et al., 2000). Subsequently, other MATE transporters have been identified and characterized (Li et al., 2002; Otsuka et al., 2005; Masuda et al., 2006). The NorM and DinF subfamily transporters are distributed in prokaryotes (**Figure 1-3**), and actively transport xenobiotics and organic cations, such as antibiotics and fluorescent dyes (**Figure 1-4**), using an electrochemical Na<sup>+</sup> or H<sup>+</sup> gradient across the membrane (Morita et al., 2000; He et al., 2004; Jin et al., 2014). MATE transporters expressed in bacterial pathogens contribute to multidrug resistance, highlighting their clinical importance (Kaatz et al., 2005; McAleese et al., 2005).

### 1.3.2 MATE transporters from *Vibrio cholerae*

*Vibrio cholerae* is a human pathogen that causes serious physical symptoms (Sjölund-Karlsson et al., 2011; Miwanda et al., 2015). Among the five families of multidrug transporters, the MATE transporters play an important role in the drug resistance of Vibrios (Begum et al., 2005). So far, six MATE homologs from *Vibrio cholerae* have been identified (see **Table 1-1**, Huda et al., 2001; Huda et al., 2003; Begum et al., 2005). VcmA (also referred to as NorM-VC) belongs to the NorM subfamily, and VcrM, VcmB, VcmD, VcmH, and VcmN belong to the DinF subfamily. Explorations of the structures and functions of *V. cholerae* MATE transporters are considered to be clinically important.

### 1.3.3 Structures and functions of MATE transporters

Over the last six years, structural and biochemical analyses of MATE transporters have been intensively pursued. To date, the crystal structures of three Na<sup>+</sup>-driven MATE transporters [*Vibrio cholerae* NorM (NorM-VC, He et al., 2010), *Neisseria gonorrhoeae* NorM (NorM-NG, Lu et al., 2013a), and *Escherichia coli* DinF subfamilies (C1bM, Mousa et al., 2016)], and two H<sup>+</sup>-driven MATE transporters [*Pyrococcus furiosus* DinF

(PfMATE, Tanaka et al., 2013) and *Bacillus halodurans* DinF subfamilies (DinF-BH, Lu et al., 2013b; Radchenko et al., 2015)] have been reported (**Figure 1-5** and **Table 1-2**). These structures revealed that the basic architecture of the prokaryotic MATE transporters consists of a unique topological arrangement of 12 transmembrane (TM) helices. These helices are divided into an N-lobe (TM1-TM6) and a C-lobe (TM7-TM12), and are arranged to form cavities within each of these lobes. The substrate-bound and cation-bound structures have provided insights into the mechanisms of substrate recognition and transport by prokaryotic MATE transporters (**Figure 1-5**).

#### 1.3.4 Two distinct transport models by H<sup>+</sup>-driven prokaryotic MATE transporters

Despite this remarkable progress on the structural front, the substrate transport mechanism by H<sup>+</sup>-driven MATE transporters has remained controversial (**Figure 1-6**). Previous structural and mutational analyses of H<sup>+</sup>-driven PfMATE suggested that H<sup>+</sup> binding to the conserved Asp41 in TM1 allosterically induces the bending of TM1, which in turn causes the shrinking of the N-lobe cavity and the release of the bound substrate. Based on this study, Tanaka *et al.* proposed the last step of the substrate extrusion mechanism (Tanaka et al., 2013; Nishima et al., 2016). In contrast, structural and

biochemical analyses of H<sup>+</sup>-driven DinF-BH suggested that H<sup>+</sup> and substrates share the conserved Asp40 in TM1 (corresponding to Asp41 of PfMATE) as the binding site, implying that H<sup>+</sup> binding directly triggers the release of the bound substrate (Lu et al., 2013b). Furthermore, because the structure of the DinF-BH D40N mutant, which is presumed to mimic the protonation of Asp40, adopted the TM1-straight conformation similar to the wild-type, it was proposed that the conformational change of TM1 does not necessarily occur during the transport cycle of DinF-BH (Radchenko et al., 2015). To address the controversy surrounding the H<sup>+</sup>-coupled substrate transport mechanism, structural analyses of other H<sup>+</sup>-driven MATE transporter homologs are needed.

### 1.3.5 Dynamics and molecular mechanism of MATE transporters

Similar to the MFS transporters (Yan, 2015), the MATE transporters are hypothesized to transport substrates by the rocker-switch mechanism (**Figure 1-1c**, He et al., 2010; Drew and Boudker, 2016), in which a binding site is alternately exposed to the intracellular and extracellular sides via distinct states (inward-open, occluded, and outward-open states). However, all of the reported MATE structures adopt a similar overall outward-open conformation. Thus, despite intensive structural analyses of MATE transporters, the conformational dynamics during the entire transport cycle, including the

last step of substrate extrusion, have remained unclear.

#### 1.4 Overview of this study

In this study, to understand the transport mechanism by H<sup>+</sup>-driven MATE transporters, the author performed the structural analysis of the crystal structures of VcmN, a MATE transporter from *Vibrio cholerae* considered to be driven by the H<sup>+</sup> gradient (Begum et al., 2005). In chapter 2, the LCP crystallization and X-ray diffraction analysis of VcmN are described in detail. The author determined the crystal structures of VcmN in two distinct conformations. In chapter 3, a structural comparison of VcmN revealed the pH-dependent conformational change of TM1. Based on these results, the common intermediates in the transport mechanism shared among the bacterial and archaeal H<sup>+</sup>-driven MATE transporters were proposed. In chapter 4, the pH-dependent conformational change of TM1 was supported by double electron-electron resonance (DEER) measurements in detergent and lipid environments. Importantly, the structural and spectroscopic analyses suggested that VcmN utilizes a transport cycle that entails the binding of lipophilic substrates via a lateral pathway from the membrane, which does not involve the generally assumed inward-open conformation. This study is summarized in chapter 5, and the general transport mechanism conserved among prokaryotic MATE transporters is discussed.

## Figures and Tables of Chapter 1

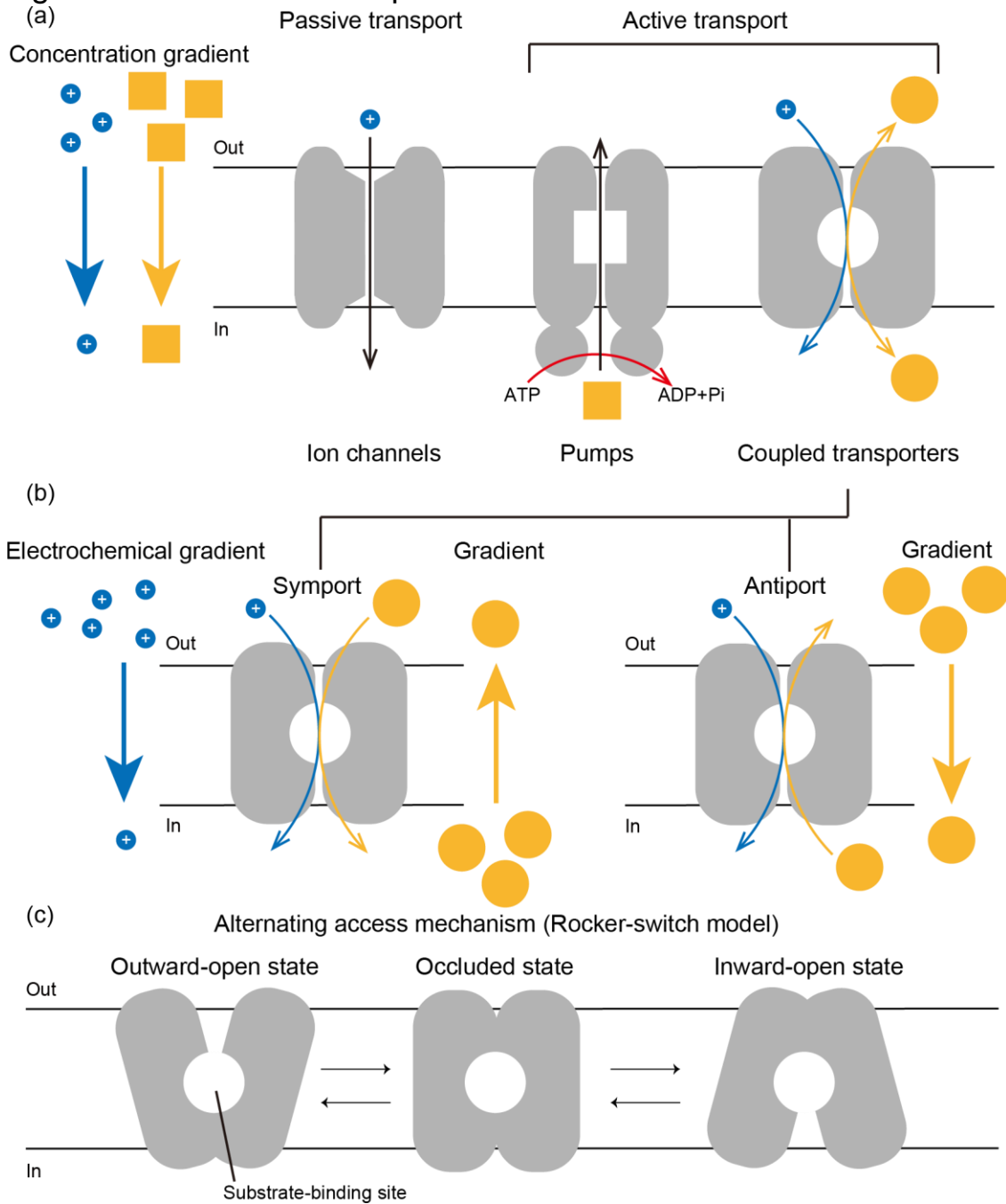


**Figure 1-1 Schematic diagram of membrane transport proteins**

(a) Passive transport and active transport. Passive transport is substrate transport in accordance with the electrochemical gradient through ion channels. Active transport is substrate transport against the electrochemical gradient. The primary active transporter is also called a “pump”. (b) Coupled transport by symporters and antiporters. The secondary active transporters are classified into the symporters and antiporters, based on the directions of the substrate flux and the coupled-ion flux. (c) Rocker-switch alternating access mechanism.

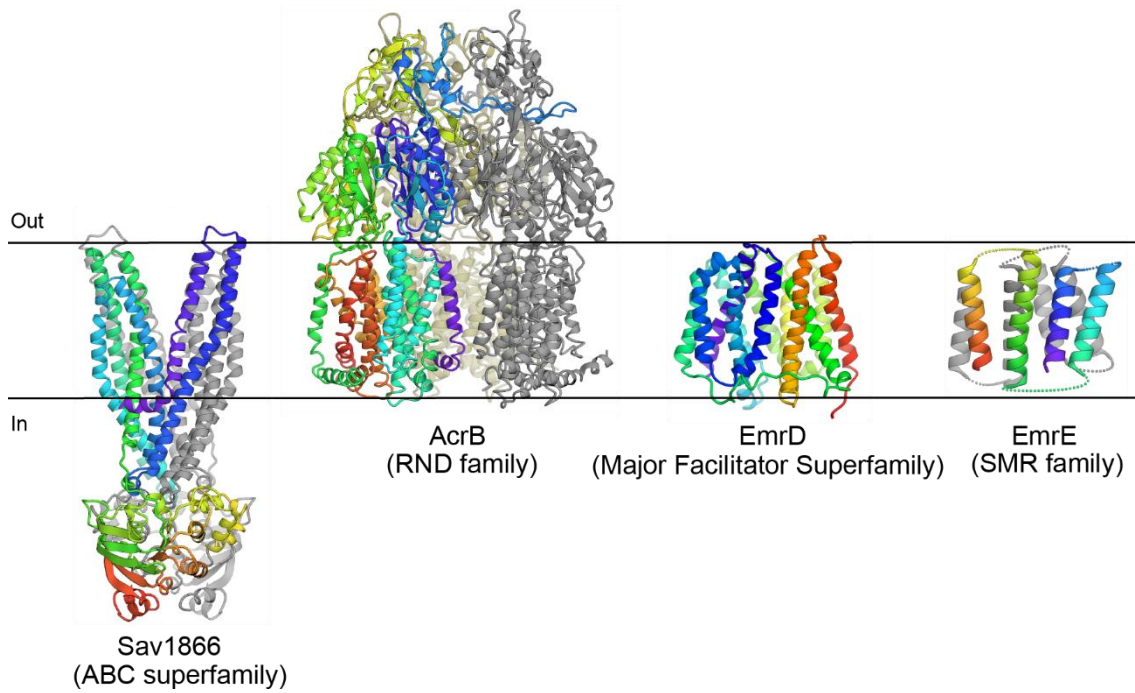


**Figure 1-2 Known multidrug transporters**

Representative structures of multidrug transporters. ABC transporter Sav1866 (PDB ID: 2HYD), RND transporter AcrB (PDB ID: 2DHH), MFS transporter EmrD (PDB ID: 2GFP), and SMR transporter EmrE (PDB ID: 2I68). The protomers of Sav1866 and EmrE are colored rainbow and grey. The protomers of AcrB are colored rainbow, grey and brown. EmrD is colored rainbow from the N-terminus (purple) to the C-terminus (red).

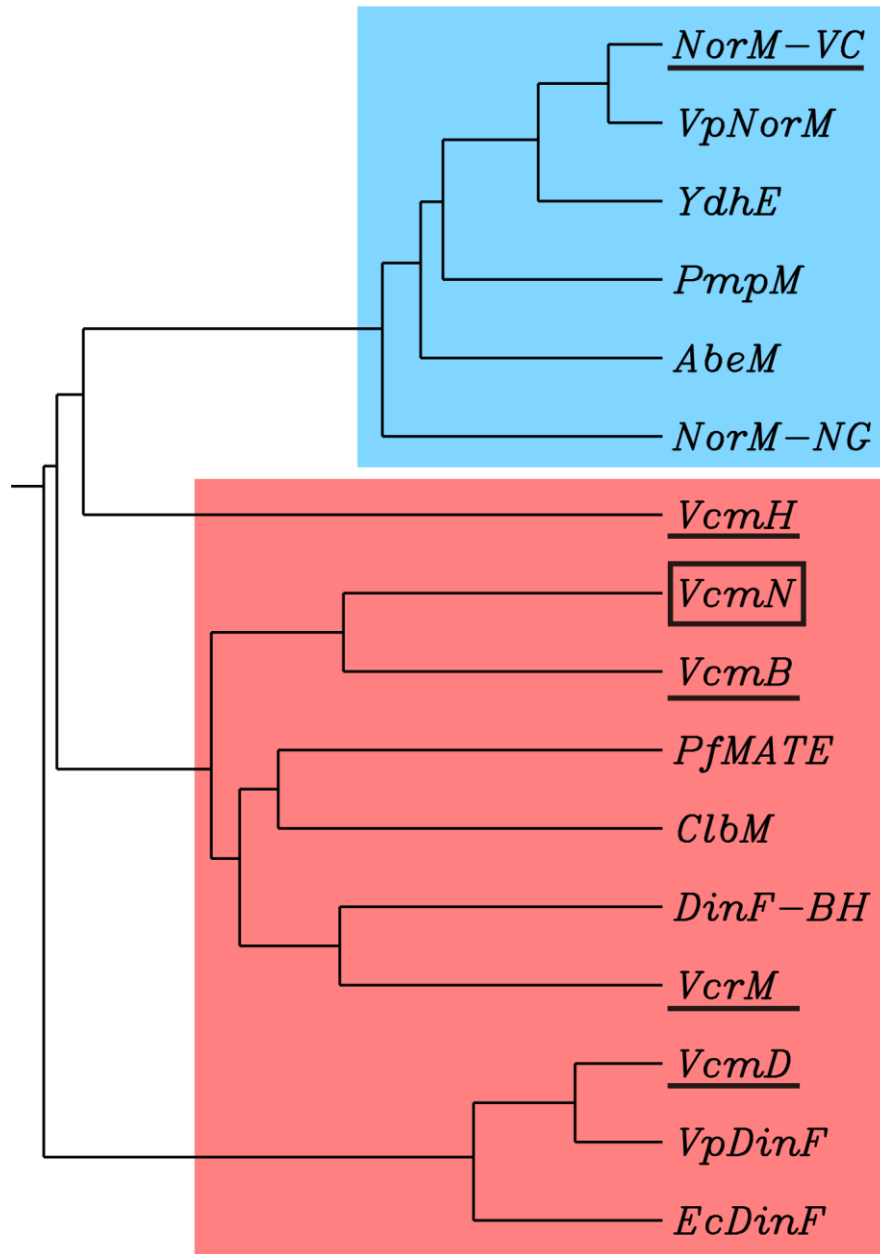


Figure 1-3 Phylogenetic tree of prokaryotic MATE transporters

A phylogenetic tree of MATE transporters from *Vibrio cholerae* and other prokaryotes. The prokaryotic MATE transporters are classified into the NorM and DinF subfamilies. The NorM and DinF subfamilies are highlighted in blue and red backgrounds, respectively. *Vibrio cholerae* MATE homologs are underlined. VcmN, the structural analysis target in this study, belongs to the DinF subfamily. YdhE, PmpM, and AbeM are NorM proteins from *Escherichia coli*, *Pseudomonas aeruginosa*, and *Acinetobacter baumannii*, respectively. Vp and Ec stand for *Vibrio parahaemolyticus* and *Escherichia coli*, respectively. The phylogenetic tree was generated using the CLUSTALW program (Thompson et al., 1994).

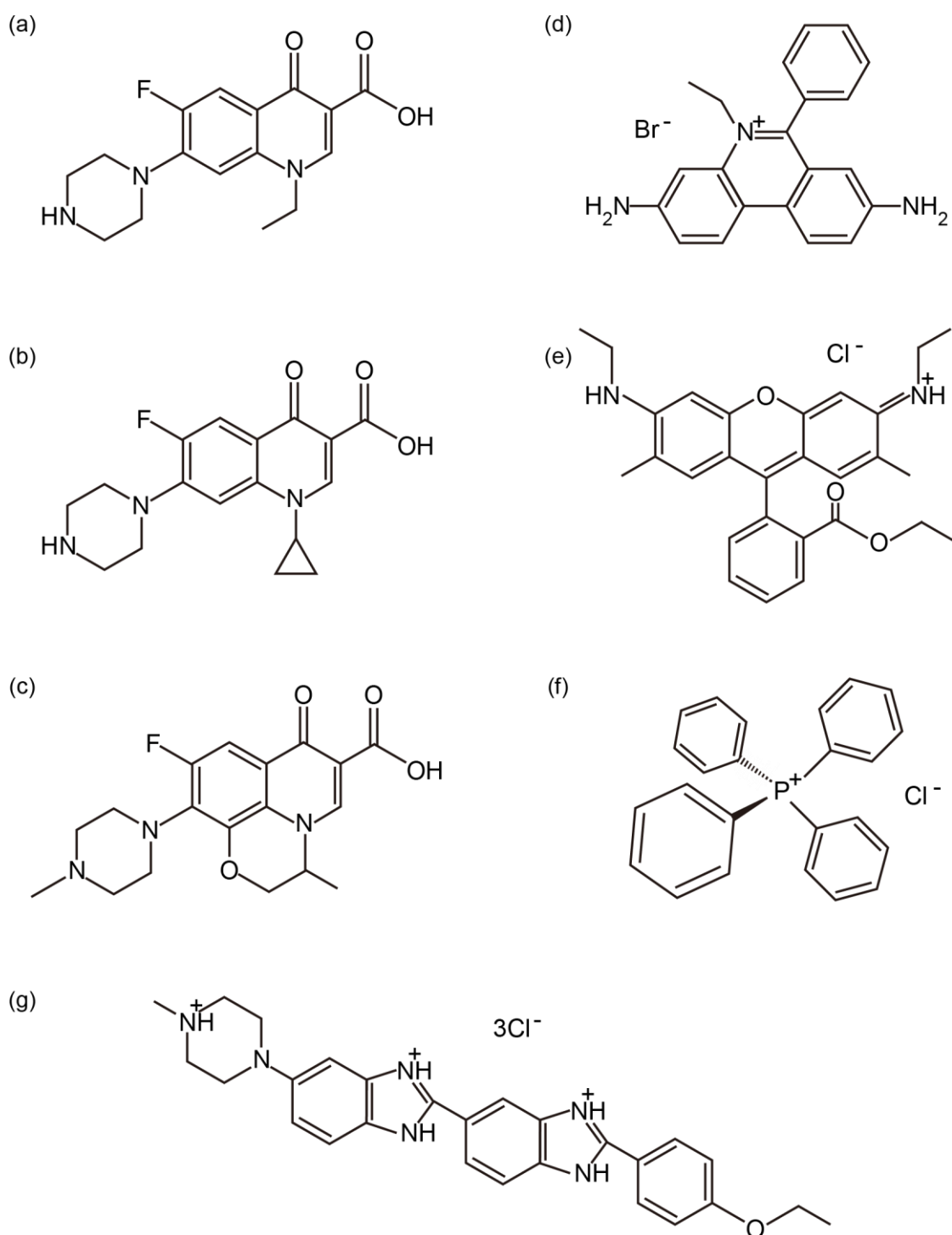
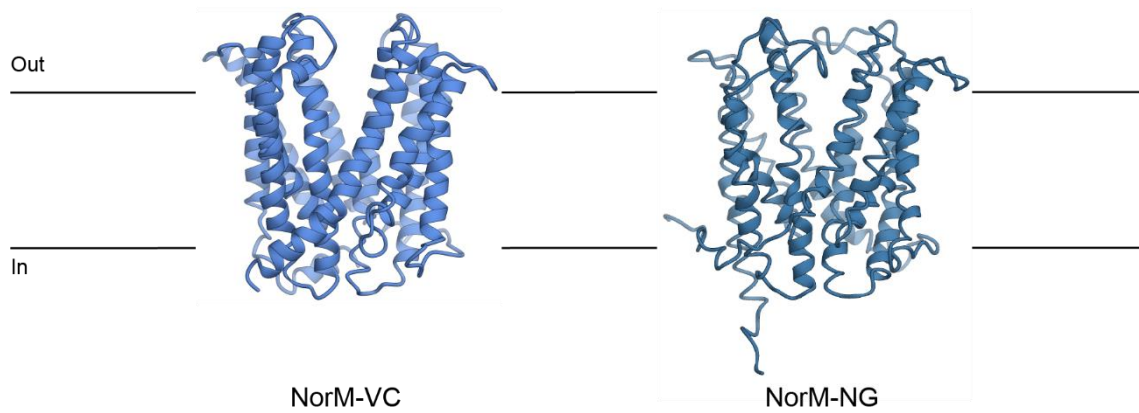


Figure 1-4 Representative substrates of MATE transporters

The structural formulae of representative substrates of MATE transporters, such as fluoroquinolones and organic cations, including (a) norfloxacin, (b) ciprofloxacin, (c) ofloxacin, (d) ethidium bromide, (e) rhodamine 6G, (f) tetraphenyl phosphonium (TPP), and (g) Hoechst 33342.

### NorM subfamily



### DinF subfamily

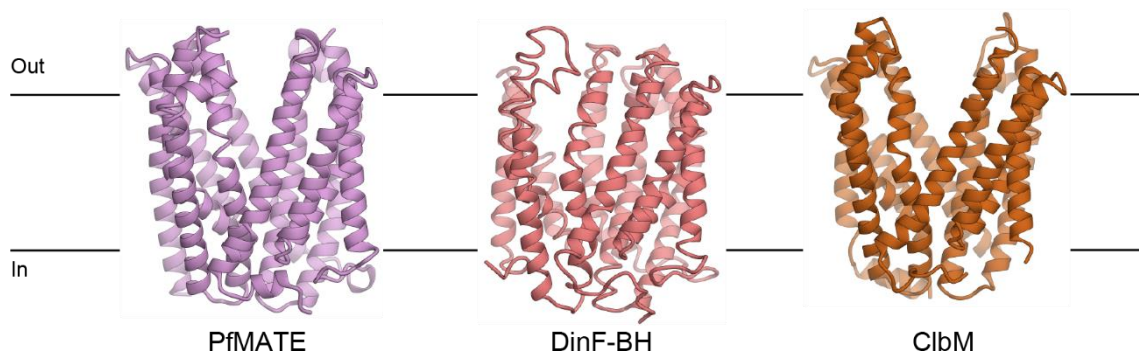


**Figure 1-5** Previously reported structures of MATE transporters

Ribbon diagrams of previously reported structures of prokaryotic MATE transporters, NorM-VC (PDB ID: 3MKT), NorM-NG (PDB ID: 4HUM), PfMATE (PDB ID: 3VVN), DinF-BH (PDB ID: 4LZ6), and ClbM (PDB ID: 4Z3N). All structures consist of 12 transmembrane helices, which are divided into the N- (TM1-TM6) and C-lobes (TM7-TM12). The central cleft formed between the N- and C-lobes is open toward the extracellular side.

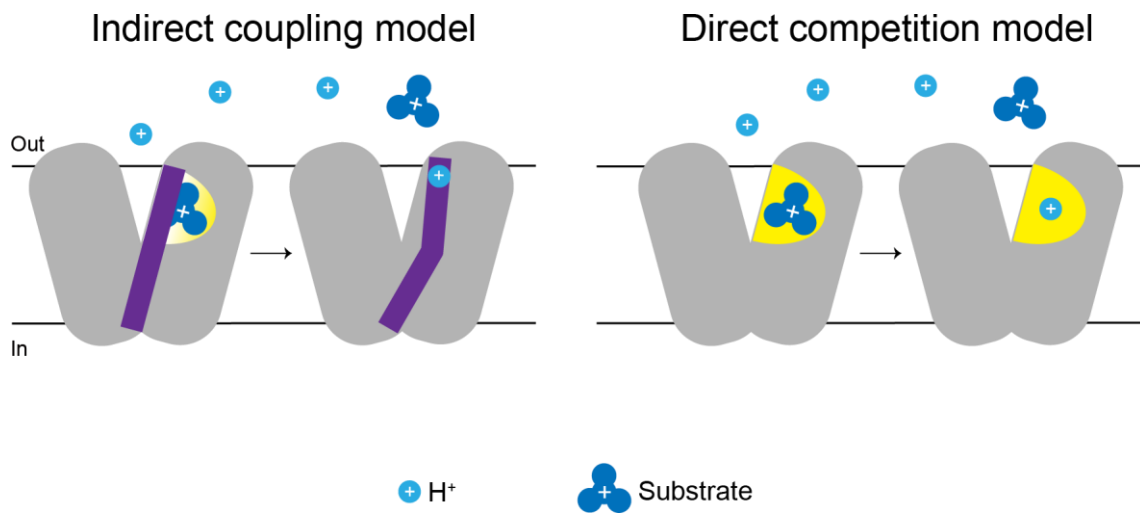


Figure 1-6 Distinct transport models of prokaryotic H<sup>+</sup>-driven transporters

Two distinct transport models for prokaryotic H<sup>+</sup>-driven transporters have been proposed. (Left) Indirect coupling model, proposed from the studies of PfMATE. (Right) Direct competition model, proposed from the studies of DinF-BH.

Table 1-1 MICs of various drugs in *E. coli* KAM32 harboring plasmid carrying each MATE gene from *Vibrio cholerae*

(Adapted from Begum *et al.*, *Microbiol. Immunol.*, 2005; Table 3)

Drugs	MIC ( $\mu\text{g/mL}$ )						
	Host: <i>E. coli</i> KAM32						
	pBR322 (control)	pMAC98 (vcmB)	pMNC4 (vcmD)	pHVC99 (vcmH)	pMTC19 (vcmN)	pMVC99 (vcmA)	pAVC33 (vcrM)
NFLX	0.015	0.06	0.06	0.12	0.06	0.5	0.015
CFLX	0.002	0.03	0.02	0.03	0.03	0.03	0.002
OFLX	0.015	0.12	0.12	0.12	0.06	0.03	0.015
KM	1	4	1	4	2	1	1
SM	1	4	1	4	2	1	2
CM	0.5	0.5	0.5	1	0.5	0.5	1
EtBr	4	8	8	8	8	16	16
Hoech	0.5	2	4	16	4	8	4

NFLX: Norfloxacin; CFLX: Ciprofloxacin; OFLX: Ofloxacin; KM: Kanamycin; SM: Streptomycin; CM: Chloramphenicol; EtBr: Ethidium bromide; Hoech: Hoechst 33342.

Table 1-2 Previously reported structures of MATE transporters

Name	Organisms	Subfamily	Driving force	Substrates / ions	Resolution (Å)	PDB IDs	Reference
NorM-VC	<i>Vibrio cholerae</i>	NorM	Na <sup>+</sup> , H <sup>+</sup>	None	3.65	3MKT	He <i>et al.</i> , <i>Nature</i> , 2010
				Rb <sup>+</sup>	4.2	3MKU	
NorM-NG	<i>Neisseria gonorrhoeae</i>	NorM	Na <sup>+</sup>	TPP	3.59	4HUK	Lu, Symersky <i>et al.</i> , <i>Proc. Natl. Acad. Sci., U.S.A.</i> , 2013
				Cs <sup>+</sup>	3.81	4HUL	
				Ethidium	3.49	4HUM	
				Rhodamine 6G	3.59	4HUN	
				Verapamil	3.0	5C6P	
ClbM	<i>Escherichia coli</i>	DinF	Na <sup>+</sup>	None	2.7	4Z3N	Mousa <i>et al.</i> , <i>Nat. Microbiol.</i> , 2016
				Rb <sup>+</sup>	3.3	4Z3P	
PfMATE	<i>Pyrococcus furiosus</i>	DinF	H <sup>+</sup>	None	2.4	3VVN	Tanaka <i>et al.</i> , <i>Nature</i> , 2013
				None	2.5	3VVO	
				Br-NRF	2.91	3VVP	
				Peptide MaD5	3.0	3VVR	
				Peptide MaD3S	2.6	3VVS	
				Peptide MaL6	2.45	3WBN	
DinF-BH	<i>Bacillus halodurans</i>	DinF	H <sup>+</sup>	None (P26A)	2.1	3W4T	Lu, Radchenko <i>et al.</i> , <i>Nat. Struct. Mol. Biol.</i> , 2013
				None	3.2	4LZ6	
				Rhodamine 6G	3.7	4LZ9	
				None (D40N)	3.0	5C6N	
				Verapamil	3.0	5C6O	

## Chapter 2 X-ray crystallographic analysis of VcmN, a MATE multidrug transporter from *Vibrio cholerae*

### 2.1 Introduction

As described in chapter 1, the substrate transport mechanism by H<sup>+</sup>-driven MATE transporters remained controversial. To elucidate the H<sup>+</sup>-driven conformational change in a MATE transporter, the author focused on one of MATE homologs from *Vibrio cholerae*, VcmN (UniProt ID: C3LWQ2, Begum et al., 2005), which is considered to be driven by the H<sup>+</sup>-gradient, and analyzed the structure of VcmN by X-ray crystallography. In this chapter, the lipidic cubic phase (LCP) crystallization and X-ray diffraction analysis of VcmN are described (Kusakizako et al., 2016).

### 2.2 Materials and Methods

#### 2.2.1 Plasmid construction

The VcmN gene was provided by Dr. Kuroda (Hiroshima University). The gene encoding full-length VcmN (UniProt ID: C3LWQ2) was subcloned into a modified pET-28a vector. This modified vector contains a C-terminal tobacco etch virus (TEV) protease cleavage site (ENLYFQG) followed by a His<sub>6</sub>-tag (**Figure 2-1a**). The secondary structure and disordered regions of VcmN were predicted using the program PSIPRED

(<http://bioinf.cs.ucl.ac.uk/psipred/>) and the program DISOPRED2 (Ward et al., 2004), respectively (**Figure 2-1b**). To improve the stability of the protein and the quality of the crystals, the ten C-terminal residues of full-length VcmN and the two vector-derived residues were truncated by a PCR-based method using PrimeSTAR Max DNA polymerase (Takara Bio) (**Figure 2-1a**). DNA fragments were amplified using DNA primers and the plasmid containing full-length VcmN as a template. The resulting DNA fragments were connected using the ligase Ligation high Ver.2 (TOYOBO). The resulting construct was designated VcmN $\Delta$ C. The macromolecule-production information and DNA primers for the construct optimization are summarized in **Table 2-1** and **Table 2-2**, respectively.

### 2.2.2 Expression and purification of VcmN

The plasmid was introduced into *Escherichia coli* C41(DE3) cells harboring pRARE, which encodes the tRNAs for codons rarely used in *E. coli*. The typical purification method is described below. The transformed cells were grown in 2.5 L of Luria-Bertani (LB) medium containing 30  $\mu\text{g mL}^{-1}$  kanamycin at 20°C. When the absorbance at 600 nm ( $A_{600}$ ) reached 0.5–0.8, expression was induced with 0.4 mM isopropyl  $\beta$ -D-1-thiogalactopyranoside (IPTG), and the cells were grown for about 20

hours at 20°C. The cells were centrifuged at  $5,000 \times g$  for 10 minutes, and disrupted by 2-3 passes at 15,000 psi using a Microfluidizer (Microfluidics). After centrifugation to remove debris at  $28,000 \times g$  for 30 minutes, the supernatant was ultracentrifuged at  $125,000 \times g$  for 1 hour, to collect the membrane fraction. The membrane fraction was resuspended in buffer A and stored at  $-80^{\circ}\text{C}$  until use. The membrane fraction was solubilized in buffer B for 1 hour at  $4^{\circ}\text{C}$ . After the removal of debris by ultracentrifugation at  $125,000 \times g$  for 30 minutes, the supernatant was mixed with 5 mL of Ni-NTA resin (QIAGEN), equilibrated with buffer C for about 1 hour at  $4^{\circ}\text{C}$ . The mixture was loaded into an Econo-column (Bio-Rad), and the flow-through fraction was discarded. The resin was washed with ten column volumes of buffer D, and the protein sample was eluted with buffer E. To cleave the His<sub>6</sub>-tag, His-tagged TEV protease (produced in-house) was added to the eluted fraction in a 10:1(w:w) protein:TEV protease ratio. During the overnight cleavage reaction at  $4^{\circ}\text{C}$ , the solution was dialyzed against buffer F. The solution was mixed with Ni-NTA resin again for 1 hour at  $4^{\circ}\text{C}$ , to remove the TEV protease. The flow-through fraction was concentrated by an Amicon Ultra centrifugal filter (50 kDa molecular weight cutoff, Millipore) and applied onto a Superdex 200 Increase 10/300 GL (GE Healthcare) column, equilibrated with buffer G. The peak fractions were concentrated to approximately  $10 \text{ mg mL}^{-1}$  by an Amicon Ultra filter (50 kDa molecular

weight cutoff, Millipore). To remove the Na<sup>+</sup> ions, a portion of the sample was dialyzed against buffer H. The purity of the protein sample was assessed by SDS-PAGE (**Figure 2-2**). Buffer compositions are summarized in **Table 2-3**.

### 2.2.3 Crystallization of VcmN

Previously, co-crystallization with macrocyclic peptides improved the quality of crystals of the selenomethionine-labeled *Pyrococcus furiosus* MATE (PfMATE), thereby facilitating its structure determination. Moreover, the macrocyclic peptides showed the inhibitory activity against PfMATE (Tanaka *et al.*, 2013; Hipolito *et al.*, 2013). Thus, to improve the quality of VcmN crystals, an *in vitro* selection of macrocyclic peptides that bind to VcmN was also performed by the random non-standard peptide integrated discovery (RaPID) system (Hipolito and Suga, 2012), in collaboration with Dr. Suga and Dr. Hipolito (The University of Tokyo). Crystallization was performed using the LCP method (Caffrey and Cherezov, 2009), as the structure of PfMATE was also determined at high resolution using this crystallization method (Tanaka *et al.*, 2013). The protein solution containing Na<sup>+</sup> was mixed with 8 mM macrocyclic peptides (**Figure 2-3a**) dissolved in dimethyl sulfoxide, in a 10:1(v/v) ratio, and the mixture was incubated for 1 hour at 4°C. The sample was mixed with monoolein (Nu-Chek Prep) in a 2:3(w:w)

protein:lipid ratio using coupled syringes. Drops of the mixture (50 nL) were dispensed onto a 96-well plastic sandwich plate (SWISSCI) and were overlaid with 600 nL reservoir solution using a Mosquito LCP crystallization robot (TTP Labtech). Initial crystallization screening was performed at 20°C using the MemMeso crystallization kit (Molecular Dimensions) and in-house-produced grid-screening crystallization kits as reservoir solutions. For crystallization optimization, StockOptions Salt and Additive Screen (Hampton Research) were added to the reservoir solutions, in addition to the optimization of the pH and the concentrations of precipitants and salts. Furthermore, 40 nL portions of a mixture of protein samples without Na<sup>+</sup> and monoolein in a 2:3(w:w) ratio were spotted on a 96-well sitting-drop plate (AS ONE) and overlaid with 800 nL reservoir solution. The obtained crystals were overlaid with 800 nL reservoir solution containing 10 mM Hoechst 33342 as a substrate (Begum et al., 2005), and were incubated at 20°C. The crystals were picked up using MicroMounts (MiTeGen) or LithoLoops (Protein Wave), and were flash-cooled in liquid nitrogen. The crystallization information is provided in **Table 2-4**.

#### 2.2.4 X-ray diffraction analysis and data processing

All X-ray diffraction data sets were collected by the helical data collection method

using a micro-focus X-ray beam at SPring-8 beamline BL32XU (Hirata et al., 2013). To reduce radiation damage, all X-ray diffraction experiments were performed under nitrogen gas stream at 100 K. Loop-harvested crystals were identified by raster scanning. A diffraction data set was collected from crystal I (described below), using a micro-focus X-ray beam (a  $1\mu\text{m}$  width  $\times$  a  $12\mu\text{m}$  height) at a wavelength of  $1.0000\text{ \AA}$  with an oscillation range of  $178^\circ$  ( $1.0^\circ$  per image), an exposure time of 1.0 s per image and an aluminium attenuator thickness of 0.6 mm. The diffracted X-ray photons were detected by an MX225HS charge coupled device (CCD) detector (Rayonix). Also, a diffraction data set was collected from crystal II (described below), using a micro-focus X-ray beam (a  $1\mu\text{m}$  width  $\times$  a  $10\mu\text{m}$  height) at a wavelength of  $1.0000\text{ \AA}$  with an oscillation range of  $180^\circ$  ( $1.0^\circ$  per image), an exposure time of 1.0 s per image and an aluminium attenuator thickness of 0.8 mm. The diffracted X-ray photons were detected by an MX225HE CCD detector (Rayonix). Each X-ray diffraction data set was collected from a single crystal. X-ray diffraction data sets were indexed, integrated and scaled by the programs XDS (Kabsch, 2010), DIALS (Waterman et al., 2013) and AIMLESS (Evans and Murshudov, 2013).

### 2.2.5 Model building and structure refinement

For phase determination, molecular replacement was performed with the program Phaser (McCoy et al., 2007) using the structure of PfMATE (PDB ID: 3VVN) as the search model. The model was manually modified using the program Coot (Emsley and Cowtan, 2004; Emsley et al., 2010) and refined using the program PHENIX refine (Adams et al., 2002; Adams et al., 2010). The Ramachandran plots were calculated by the program RAMPAGE (Lovell et al., 2003).

## 2.3 Results and Discussion

### 2.3.1 Expression, purification and construct optimization of VcmN

In general, the expression level and stability of the protein sample are important factors for structural analysis. The author first overexpressed and purified the full-length VcmN. However, the full-length VcmN partially precipitated during the concentration step. In addition, the size-exclusion chromatography (SEC) chromatogram peak was not monodisperse, thus indicating instability of full-length VcmN. To improve the stability, the C-terminal 12 residues of full-length VcmN were truncated as the C-terminal residues of VcmN were predicted to be disordered, based on a DISOPRED2 analysis (**Figure 2-1b**, Ward et al., 2004). During the purification of VcmN $\Delta$ C, the loss of sample by

aggregation was suppressed compared with that of the full-length protein, and the SEC chromatogram peak showed monodispersity. The final yield increased from 1 to 5 mg per 2.5 L culture on truncating the C-terminal 12 residues. The SEC chromatograms and the Coomassie Brilliant Blue (CBB)-stained gel are shown in **Figure 2-2**.

### 2.3.2 Crystallization of VcmN

An LCP crystallization screening of VcmN $\Delta$ C was performed. Initially, tiny crystals of the mixture of VcmN $\Delta$ C and the macrocyclic peptide (**Figure 2-3a**) were obtained under several conditions containing precipitants such as polyethylene glycol (PEG) 300 and PEG 400 using sandwich plates. As a result of optimization efforts, including the screening of additives using StockOptions Salt and Additive Screen kits, rectangular prism-shaped crystals were obtained in a reservoir solution composed of 30% PEG 300, 100 mM sodium citrate pH 5.0, and 100 mM ammonium fluoride (**Figure 2-3b**). Crystals appeared in a day and grew to approximate dimensions of  $10 \times 10 \times 25 \mu\text{m}$  in a week. The author also attempted crystallization of VcmN $\Delta$ C without the macrocyclic peptides. In contrast to the crystallization of PfMATE, the author unfortunately found that the peptides did not affect the quality of the VcmN $\Delta$ C crystals. Next, crystallization screening was performed using sitting-drop plates. In contrast to crystallization in

sandwich plates, crystallization in sitting-drop plates is suitable for substrate-soaking experiments, to determine the structures of complexes with substrates. Rod-shaped crystals were obtained in a reservoir composed of 30% PEG 500 dimethyl ether (DME), 100 mM Tris-HCl pH 8.0, and 100 mM magnesium formate. The approximate dimensions of the crystals were  $10 \times 10 \times 50 \mu\text{m}$  (**Figure 2-3c**). The sizes of the crystals obtained in the sitting-drop plates were usually larger than those produced in the sandwich plates. Finally, as a result of the optimization of the salt concentration and the pH condition, crystals with approximate dimensions of  $10 \times 10 \times 100 \mu\text{m}$  were obtained in reservoir solutions composed of 28–33% PEG 500 DME, 100 mM Tris-HCl pH 7.5, and 50 mM magnesium formate (**Figure 2-3d**). For the substrate-soaking experiments, an 800 nL portion of reservoir solution containing 10 mM Hoechst 33342 was added to drops containing crystals. The protein crystals were incubated for about one month at 20°C and then cooled in liquid nitrogen. The crystals obtained under pH 7.5–8.0 and pH 5.0 conditions designated crystals I and II, respectively (**Table 2-4**).

### 2.3.3 X-ray diffraction analysis

Crystal I diffracted X-rays to 2.2 Å resolution (**Figure 2-4a**) and belonged to the space group  $P2_12_12_1$ , with unit cell parameters of  $a = 62.2$ ,  $b = 92.0$ ,  $c = 101.3 \text{ \AA}$ . The

calculated Matthew's coefficient is  $3.05 \text{ \AA}^3 \text{ Da}^{-1}$  with 59.7% solvent content, assuming the presence of one molecule of the asymmetric unit (**Figure 2-5a**). Crystal II diffracted X-rays to  $2.5 \text{ \AA}$  resolution (**Figure 2-4b**), and belonged to the space group  $P2_12_12_1$ , with unit cell parameters of  $a = 52.3$ ,  $b = 93.7$ ,  $c = 100.2 \text{ \AA}$ . The calculated Matthew's coefficient is  $2.58 \text{ \AA}^3 \text{ Da}^{-1}$  with 52.4% solvent content, assuming the presence of one molecule in the asymmetric unit (**Figure 2-5b**).

#### 2.3.4 Phase determination, model building and structure refinement

Molecular replacement was performed using the structure of PfMATE as the search model, and thus interpretable electron density maps were obtained. However, the author did not observe an electron density peak corresponding to either the macrocyclic peptide or Hoechst 33342. The final models of the form I structure ( $2.2 \text{ \AA}$  resolution,  $R_{\text{work}} / R_{\text{free}} = 0.1980 / 0.2405$ ) and the form II structure ( $2.5 \text{ \AA}$  resolution,  $R_{\text{work}} / R_{\text{free}} = 0.2350 / 0.2672$ ) were refined using data sets from crystals I and II, respectively. The electron density maps of the form I and II structures after refinement are shown in **Figure 2-6** and **Figure 2-7**, respectively. The stereochemical quality of the models was validated by Ramachandran plot analysis (**Figure 2-8**). The crystal packing of VcmN in crystals I and II are shown in **Figure 2-9**. Data collection and refinement statistics are shown in **Table 2-5**.

## Figures and Tables of Chapter 2

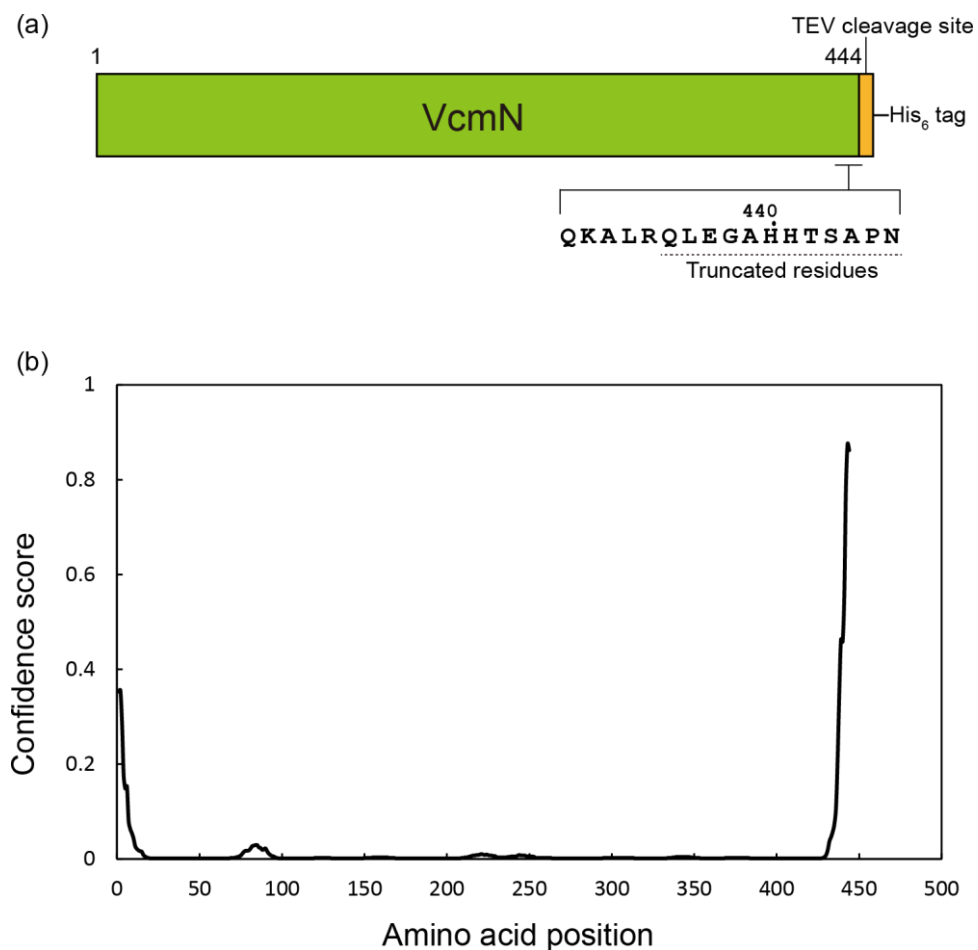
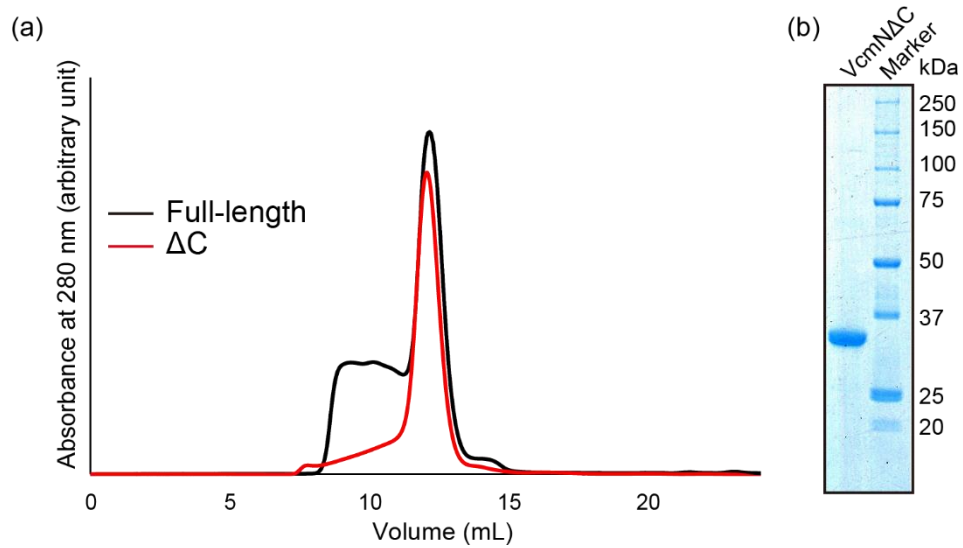


Figure 2-1 Schematic diagram of the VcmN crystallization construct

(a) Expression constructs of full-length VcmN and C-terminally truncated VcmN. The TEV protease cleavage site and a His<sub>6</sub>-tag were fused into the C-terminus of inserted gene. (b) Disordered probability of amino acids of VcmN predicted using the program DISOPRED2 (Ward et al., 2004).



**Figure 2-2 Size-exclusion chromatograms and SDS-PAGE analysis**

(a) Chromatograms of full-length VcmN and VcmN $\Delta$ C. (b) SDS-PAGE analysis with coomassie brilliant blue staining. Left lane, VcmN $\Delta$ C; right lane, molecular-weight markers (labeled in kDa).

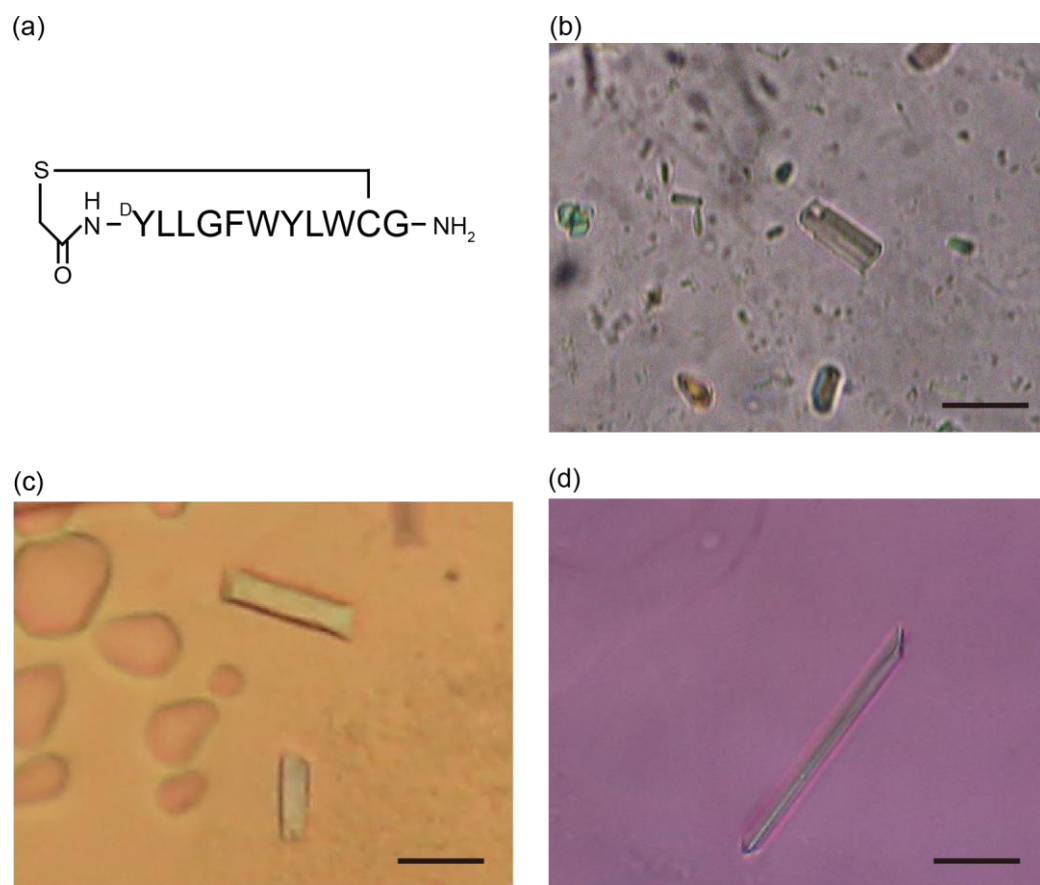


Figure 2-3 Crystals of VcmNΔC

(a) Schematic representation of the macrocyclic peptide. Crystals obtained under the different pH conditions. Crystal II (b) and crystal I (c, d), respectively. The scale bars represent 30 μm.

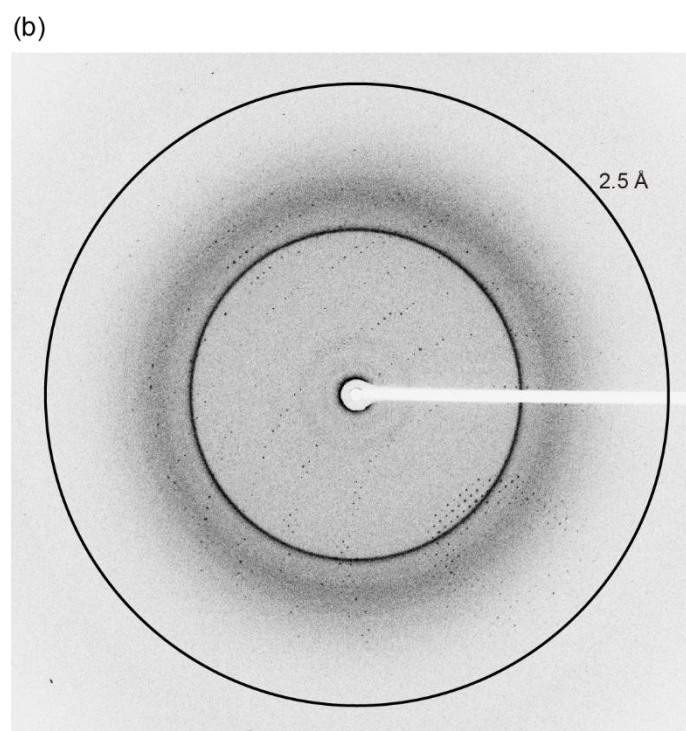
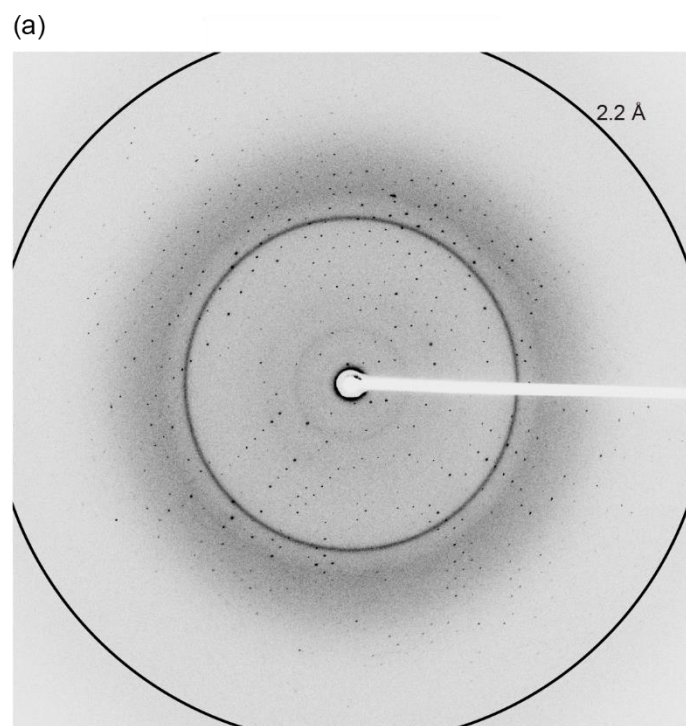


Figure 2-4 X-ray diffraction images

X-ray diffraction images of crystals I **(a)** and II **(b)**. The rings indicate 2.2 Å **(a)** and 2.5 Å **(b)** resolution, respectively.

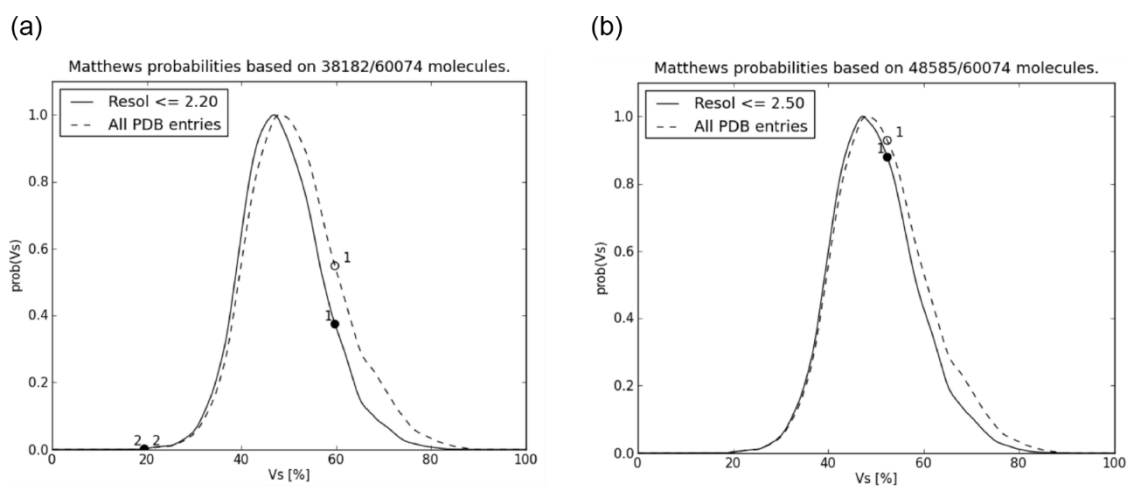


Figure 2-5 Matthew's coefficient

Matthew's coefficients were predicted from the space group, cell dimensions and molecular weight of VcmNAC, and are shown on the probability distribution of Matthew's coefficients from deposited to Protein Data Bank (PDB). The probabilities are maximum, assuming the presence of one molecule in the asymmetric unit of both crystals I (a) and II (b).

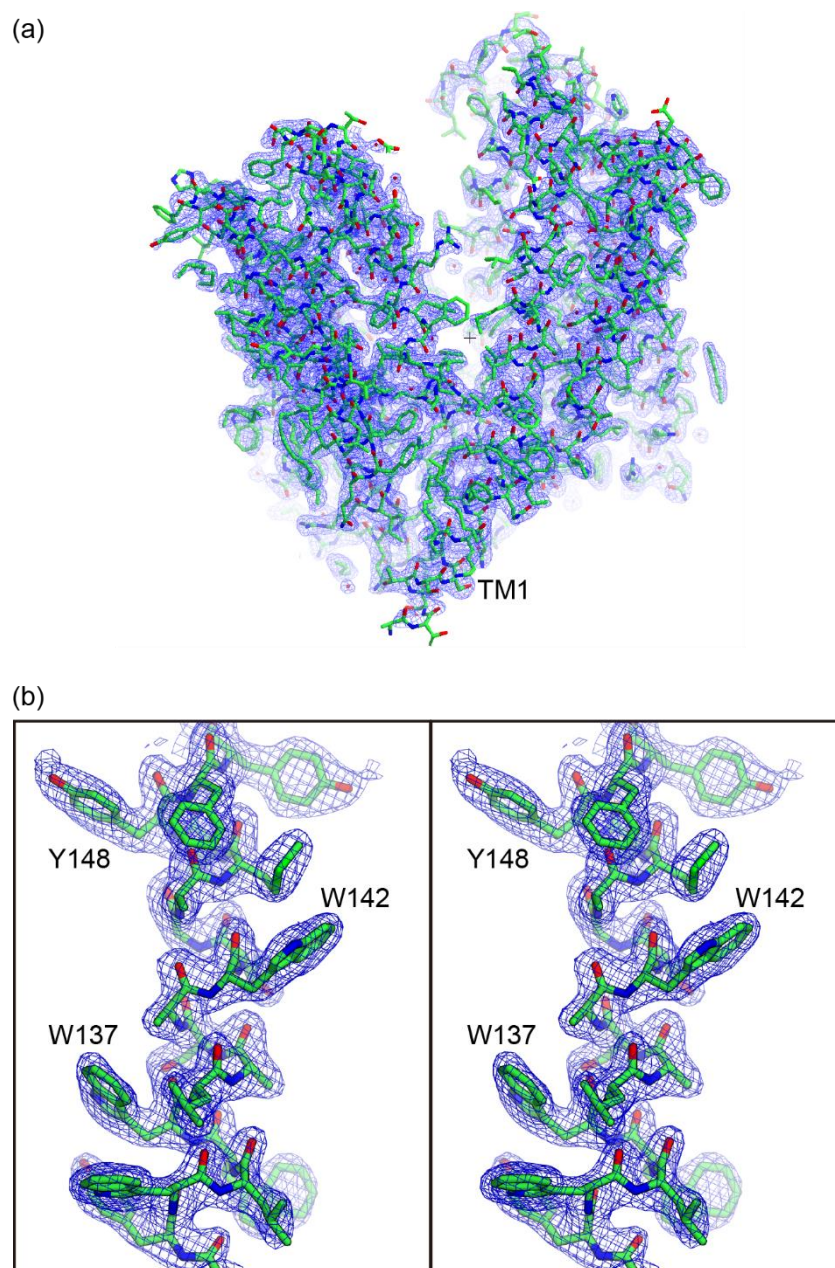


Figure 2-6 Electron density map (Form I)

The  $2F_o-F_c$  electron density maps of the overall structure (a) and the TM4 helix (b, stereoview), contoured at  $1.0 \sigma$ .

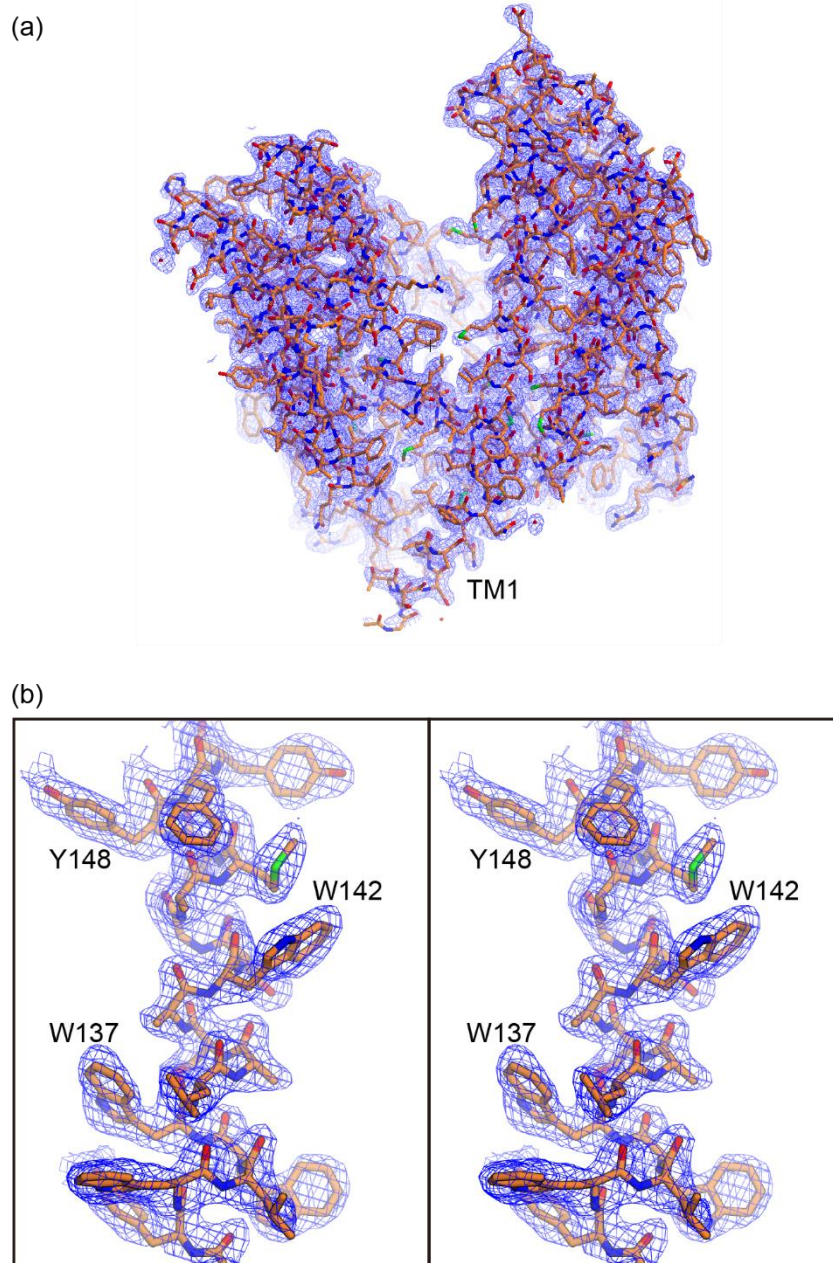


Figure 2-7 Electron density map (Form II)

The  $2Fo-Fc$  electron density maps of the overall structure (a) and the TM4 helix (b, stereoview), contoured at  $1.0 \sigma$ .

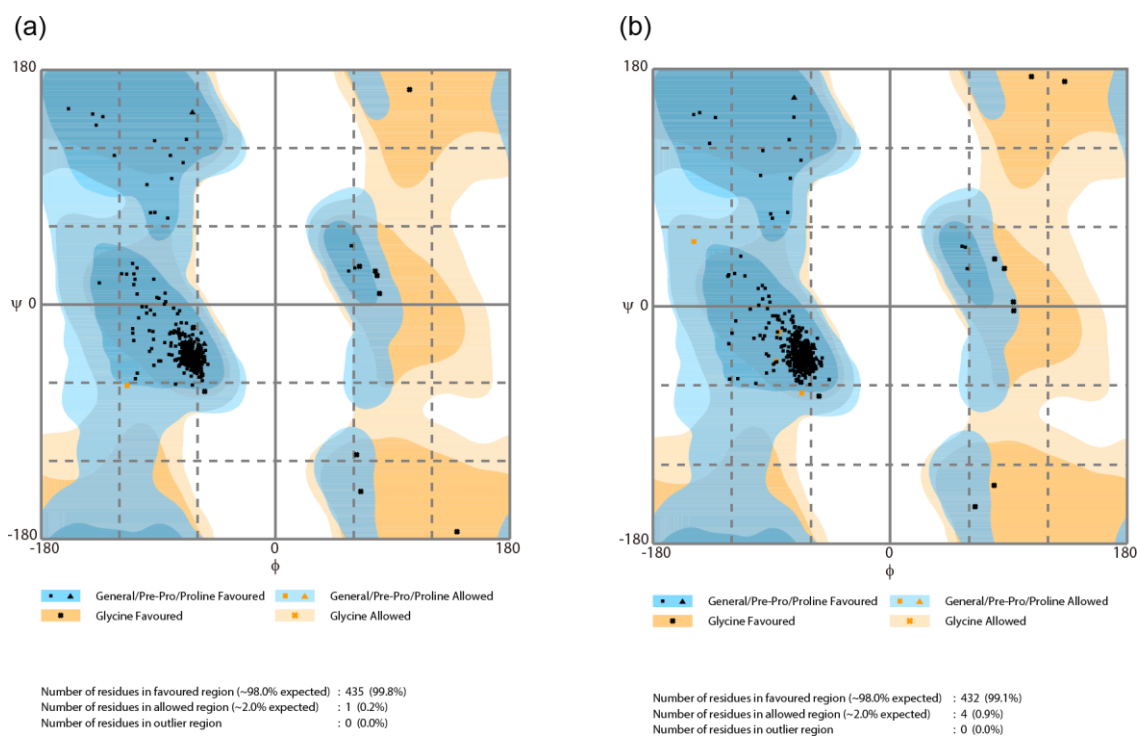
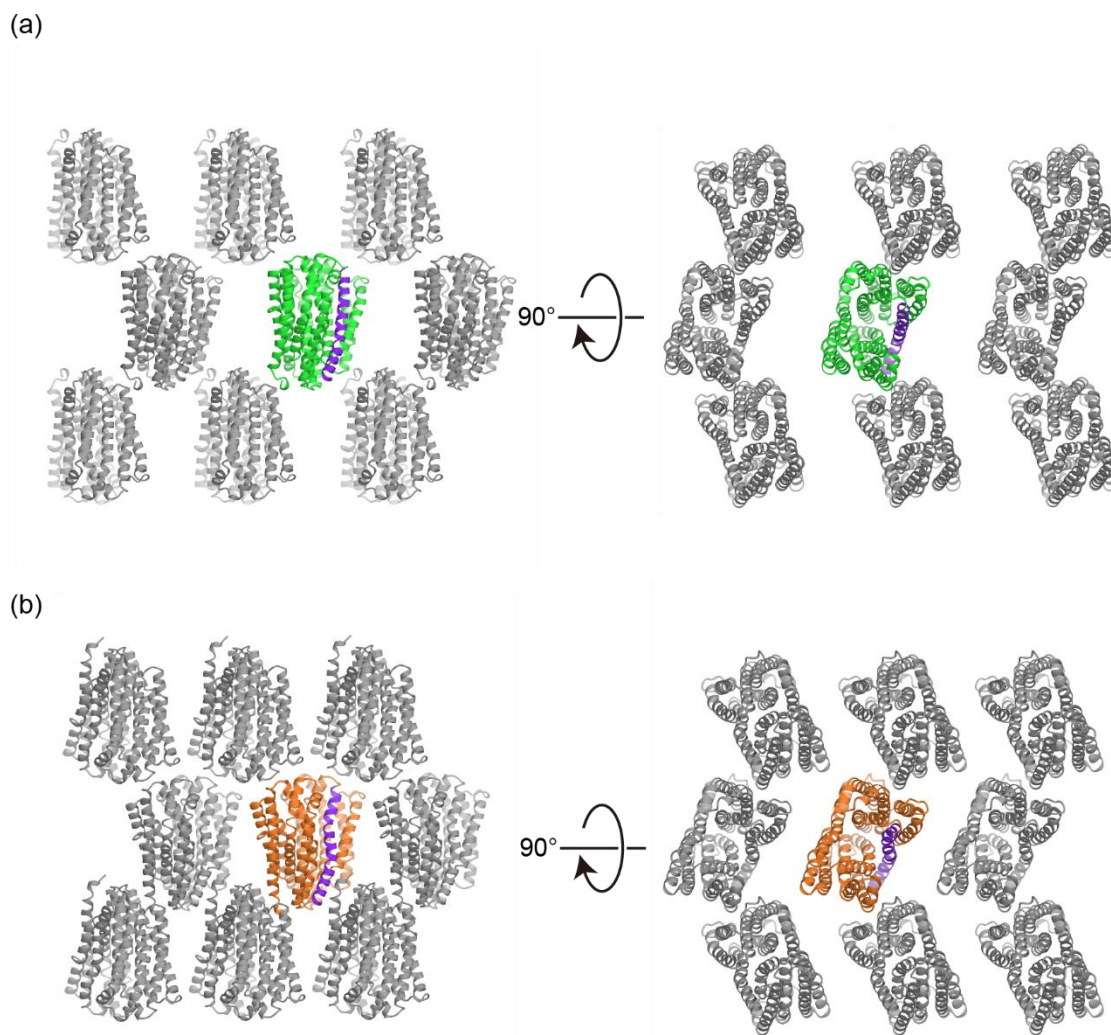


Figure 2-8 Ramachandran plots

Ramachandran plots of crystal I (a) and crystal II (b) structures.



**Figure 2-9 Crystal packing**

The molecules in the asymmetric unit of crystals I **(a)** and II **(b)** are colored green and orange, respectively. The crystal packing, viewed from the membrane side (left) and the extracellular side (right). The TM1 helix of both crystals is highlighted in purple.

Table 2-1 Macromolecule-production information

Source organism	<i>Vibrio cholerae</i>
DNA source	UniProt ID: C3LWQ2
Expression vector	Modified pET-28a
Expression host	<i>E. coli</i> strain C41(DE3) Rosetta
Amino acid sequence of the construct	<p><u>M</u><u>A</u><u>M</u>Q T S T S S L A K Q L F Q M T W P M L F G V L S L M S F Q L V D S A F I G Q L</p> <p>G V L P L A A Q G F T M P I Q M V I I G I Q V G L G I A T T A V I S R A I G A G K T E Y</p> <p>A K Q L G G L V I V I G G I G V A L I A L V L Y L L R Q P L L G L L G A P E T V F A I I D</p> <p>H Y W L W W L A S A W T G A M L Y F Y Y S V C R A N G N T L L P G T L M M V T S</p> <p>V L N L I L D P I F I F T F D L G I D G A A I A T I I A F G V G I A I V A P K V A Q R Q W T</p> <p>S Y Q W Q D L N I S Q S L T A L G H I M G P A M L S Q L L P P L S S M F A T K L L A S</p> <p>F G T A A V A A W A L G S R F E F F A L V A V L A M T M S L P P M I G R M L G A K E I</p> <p>T H I R Q L V R I A C Q F V L G F Q L L I A L V T Y V F A T P L A E L M T S E T E V S Q I</p> <p>L N L H L V I V P I S L G A L G I C M L M V S V A N A L G K S Y V A L T I S A L R L F A</p> <p>F Y L P C L W L G A H F Y G I E G L F I G A L V G N I I A G W A A W L A Y Q K A L R (</p> <p><u>Q L E G A H H T S A P N</u>) <u>S E N L Y F Q G Q V D K L A A A L E H H H H H H</u></p>

The cloning artifacts are underlined. The truncated residues are in parentheses.

Table 2-2 DNA primers for construct optimization

Mutants	Fw / Rv	Sequence (5'→3')
ΔC	Fw	TCGGAAAATTTATATTTTCAAGGTC
	Rv	ACGTAAAGCTTTTTGATAAGCG

Table 2-3 Buffer composition

Name	Composition
Buffer A	20 mM Tris-HCl pH 8.0, 300 mM NaCl
Buffer B	20 mM Tris-HCl pH 8.0, 300 mM NaCl, 1.5% n-dodecyl-β-D-maltopyranoside (DDM), 20 mM imidazole
Buffer C	20 mM Tris-HCl pH 8.0, 300 mM NaCl, 0.1% DDM, 20 mM imidazole
Buffer D	20 mM Tris-HCl pH 8.0, 300 mM NaCl, 0.1% DDM, 30 mM imidazole
Buffer E	20 mM Tris-HCl pH 8.0, 300 mM NaCl, 0.1% DDM, 300 mM imidazole
Buffer F	20 mM Tris-HCl pH 8.0, 300 mM NaCl, 0.02% DDM
Buffer G	20 mM Tris-HCl pH 8.0, 100 mM NaCl, 0.1% DDM
Buffer H	20 mM Tris-HCl pH 8.0, 0.02% DDM

Table 2-4 Crystallization conditions

	Crystal I	Crystal II
Method	Lipidic cubic phase	Lipidic cubic phase
Plate type	96-well sitting-drop plate	96-well plastic sandwich plate
Temperature (°C)	20	20
Protein concentration (mg mL <sup>-1</sup> )	10	10
Buffer composition of protein solution	20 mM Tris-HCl pH 8.0, 0.02% DDM	20 mM Tris-HCl pH 8.0, 100 mM NaCl 0.1% DDM
Co-crystallized compound (final concentration in mixture with protein solution)	–	0.8 mM macrocyclic peptide
Composition of reservoir solution	28–33% PEG 500 DME 100 mM Tris-HCl pH 7.5–8.0, 50–100 mM magnesium formate	30% PEG 300 100 mM sodium citrate pH 5.0 100 mM ammonium fluoride
Volume of LCP drop (nL)	40	50
Volume of reservoir (nL)	800	600
Soaked compound (final concentration in crystallization drop)	5 mM Hoechst 33342	–

Table 2-5 Data collection statistics

	VcmN (form I, straight)	VcmN (form II, bent)
<b>Data collection</b>		
Diffraction source	SPring-8 BL32XU	SPring-8 BL32XU
Wavelength (Å)	1.0000	1.0000
Temperature (K)	100	100
Detector	Rayonix MX225HS	Rayonix MX225HE
Crystal-to-detector distance (mm)	240	240
Rotation range per image (°)	1.0	1.0
Total rotation range (°)	178	180
Exposure time per image (s)	1.0	1.0
Thickness of aluminium attenuator (mm)	0.6	0.8
Space group	$P2_12_12_1$	$P2_12_12_1$
$a, b, c$ (Å)	62.2, 92.0, 101.3	52.3, 93.7, 100.2
Resolution (Å)	46.0–2.21 (2.34–2.21)	93.7–2.50 (2.60–2.50)
$R_{\text{meas}}$	0.167 (1.397)	0.252 (0.995)
$I/\sigma I$	10.5 (1.4)	5.9 (1.9)
Completeness (%)	99.6 (97.9)	99.8 (98.5)
Redundancy	7.0 (5.7)	6.7 (5.9)
$CC_{1/2}$	0.997 (0.539)	0.989 (0.635)

Values in parentheses are for the highest resolution shell.

Table 2-6 Refinement statistics

	VcmN (form I, straight)	VcmN (form II, bent)
<b>Refinement</b>		
Resolution (Å)	46.0–2.2	68.5–2.5
No. of reflections	29,916	17,610
$R_{\text{work}} / R_{\text{free}}$	0.1980 / 0.2405	0.2350 / 0.2672
No. of atoms		
Protein	3,316	3,250
Ligand	195	35
Water	89	35
<i>B</i> -factors		
Protein	46.50	34.80
Ligand	59.30	36.50
Water	45.40	30.10
R.m.s deviations		
Bond length (Å)	0.003	0.003
Bond angles (°)	0.78	0.78
Ramachandran plot (%)		
Favored region	99.8	99.1
Allowed region	0.2	0.9
Outlier region	0.0	0.0

## Chapter 3 Crystal structures of VcmN

This chapter is not published because it is scheduled to be published in journals within five years.

## Chapter 4 Dynamics analysis of VcmN using DEER spectroscopy

This chapter is not published because it is scheduled to be published in journals within five years.

## Chapter 5 General Discussion

This chapter is not published because it is scheduled to be published in journals within five years.

## References

- Adams, P.D., Grosse-Kunstleve, R.W., Hung, L.W., Ioerger, T.R., McCoy, A.J., Moriarty, N.W., Read, R.J., Sacchettini, J.C., Sauter, N.K., and Terwilliger, T.C. (2002). PHENIX: Building new software for automated crystallographic structure determination. *Acta Crystallographica Section D: Biological Crystallography* 58, 1948–1954.
- Adams, P.D., Afonine, P. V., Bunkóczi, G., Chen, V.B., Davis, I.W., Echols, N., Headd, J.J., Hung, L.W., Kapral, G.J., Grosse-Kunstleve, R.W., et al. (2010). PHENIX: A comprehensive Python-based system for macromolecular structure solution. *Acta Crystallographica Section D: Biological Crystallography* 66, 213–221.
- Aller, S.G., Yu, J., Ward, A., Weng, Y., Chittaboina, S., Zhuo, R., Harrell, P.M., Trinh, Y.T., Zhang, Q., Urbatsch, I.L., et al. (2009). Structure of P-Glycoprotein Reveals a Molecular Basis for Poly-Specific Drug Binding. *Science* 323, 1718 LP-1722.
- Bay, D.C., Rommens, K.L., and Turner, R.J. (2008). Small multidrug resistance proteins: A multidrug transporter family that continues to grow. *Biochimica et Biophysica Acta - Biomembranes* 1778, 1814–1838.
- Begum, A., Rahman, M.M., Ogawa, W., Mizushima, T., Kuroda, T., and Tsuchiya, T. (2005). Gene cloning and characterization of four MATE family multidrug efflux pumps from *Vibrio cholerae* non-O1. *Microbiology and Immunology* 49, 949–957.
- Brown, M.H., Paulsen, I.T., and Skurray, R.A. (1999). The multidrug efflux protein NorM is a prototype of a new family of transporters. *Molecular Microbiology* 31, 394–395.
- Caffrey, M., and Cherezov, V. (2009). Crystallizing membrane proteins using lipidic mesophases. *Nature Protocols* 4, 706–731.
- Chen, C. jie, Chin, J.E., Ueda, K., Clark, D.P., Pastan, I., Gottesman, M.M., and Roninson, I.B. (1986). Internal duplication and homology with bacterial transport proteins in the *mdr1* (P-glycoprotein) gene from multidrug-resistant human cells. *Cell* 47, 381–389.
- Chen, Y.-J., Pornillos, O., Lieu, S., Ma, C., Chen, A.P., and Chang, G. (2007). X-ray structure of EmrE supports dual topology model. *Proceedings of the National Academy of Sciences of the United States of America* 104, 18999–19004.
- Claxton, D.P., Quick, M., Shi, L., de Carvalho, F.D., Weinstein, H., Javitch, J. a, and McHaourab, H.S. (2010). Ion/substrate-dependent conformational dynamics of a bacterial homolog of neurotransmitter:sodium symporters. *Nature Structural & Molecular Biology* 17, 822–829.
- Claxton, D.P., Kazmier, K., Mishra, S., and McHaourab, H.S. (2015). Navigating Membrane Protein Structure, Dynamics, and Energy Landscapes Using Spin Labeling and EPR Spectroscopy (Elsevier Inc.).
- Dastvan, R., Fischer, A.W., Mishra, S., Meiler, J., and Mchaourab, H.S. (2015). Protonation-Dependent Conformational Dynamics of the Multidrug Transporter EmrE. *Proceedings*

- of the National Academy of Sciences (Accepted) *113*, 1220–1225.
- Dawson, R.J.P., and Locher, K.P. (2006). Structure of a bacterial multidrug ABC transporter. *Nature* *443*, 180–185.
- Deng, D., Sun, P., Yan, C., Ke, M., Jiang, X., Xiong, L., Ren, W., Hirata, K., Yamamoto, M., Fan, S., et al. (2015). Molecular basis of ligand recognition and transport by glucose transporters. *Nature* *526*, 391–396.
- Dolinsky, T.J., Czodrowski, P., Li, H., Nielsen, J.E., Jensen, J.H., Klebe, G., and Baker, N.A. (2007). PDB2PQR: Expanding and upgrading automated preparation of biomolecular structures for molecular simulations. *Nucleic Acids Research* *35*, 522–525.
- Drew, D., and Boudker, O. (2016). Shared Molecular Mechanisms of Membrane Transporters. *Annual Review of Biochemistry* *85*, 543–572.
- Emsley, P., and Cowtan, K. (2004). Coot: Model-building tools for molecular graphics. *Acta Crystallographica Section D: Biological Crystallography* *60*, 2126–2132.
- Emsley, P., Lohkamp, B., Scott, W.G., and Cowtan, K. (2010). Features and development of Coot. *Acta Crystallographica Section D: Biological Crystallography* *66*, 486–501.
- Evans, P.R., and Murshudov, G.N. (2013). How good are my data and what is the resolution? *Acta Crystallographica Section D: Biological Crystallography* *69*, 1204–1214.
- Fukuda, M., Takeda, H., Kato, H.E., Doki, S., Ito, K., Maturana, A.D., Ishitani, R., and Nureki, O. (2015). Structural basis for dynamic mechanism of nitrate/nitrite antiport by NarK. *Nature Communications* *6*, 7097.
- Hassan, K.A., Jackson, S.M., Penesyan, A., Patching, S.G., Tetu, S.G., and Eijkelkamp, B.A. (2013). Transcriptomic and biochemical analyses identify a family of chlorhexidine efflux proteins. *110*, 1–6.
- Hassan, K.A., Liu, Q., Henderson, P.J.F., and Paulsen, I.T. (2015). Homologs of the *Acinetobacter baumannii* acei transporter represent a new family of bacterial multidrug efflux systems. *mBio* *6*, 1–5.
- He, G., Kuroda, T., Mima, T., Morita, Y., and Mizushima, T. (2004). An H<sup>+</sup>-Coupled Multidrug Efflux Pump, PmpM, a Member of the MATE Family of Transporters, from *Pseudomonas aeruginosa*. *Journal of Bacteriology* *186*, 262–265.
- He, X., Szewczyk, P., Karyakin, A., Evin, M., Hong, W.-X., Zhang, Q., and Chang, G. (2010). Structure of a cation-bound multidrug and toxic compound extrusion transporter. *Nature* *467*, 991–994.
- Hipolito, C.J., and Suga, H. (2012). Ribosomal production and in vitro selection of natural product-like peptidomimetics: The FIT and RaPID systems. *Current Opinion in Chemical Biology* *16*, 196–203.
- Hipolito, C.J., Tanaka, Y., Katoh, T., Nureki, O., and Suga, H. (2013). A macrocyclic peptide that

- serves as a cocrystallization ligand and inhibits the function of a MATE family transporter. *Molecules* *18*, 10514–10530.
- Hirata, K., Kawano, Y., Ueno, G., Hashimoto, K., Murakami, H., Hasegawa, K., Hikima, T., Kumasaka, T., and Yamamoto, M. (2013). Achievement of protein micro-crystallography at SPring-8 beamline BL32XU. *Journal of Physics: Conference Series* *425*, 12002.
- Hopf, T.A., Colwell, L.J., Sheridan, R., Rost, B., Sander, C., and Marks, D.S. (2012). Three-dimensional structures of membrane proteins from genomic sequencing. *Cell* *149*, 1607–1621.
- Huda, M.N., Morita, Y., Kuroda, T., Mizushima, T., and Tsuchiya, T. (2001). Na<sup>+</sup>-driven multidrug efflux pump VcmA from *Vibrio cholerae* non-O1, a non-halophilic bacterium. *FEMS Microbiology Letters* *203*, 235–239.
- Huda, M.N., Chen, J., Morita, Y., Kuroda, T., Mizushima, T., and Tsuchiya, T. (2003). Gene cloning and characterization of VcrM, a Na<sup>+</sup>-coupled multidrug efflux pump, from *Vibrio cholerae* non-O1. *Microbiology and Immunology* *47*, 419–427.
- Ishima, R., and Torchia, D. (2000). Protein dynamics from NMR. *Nature Structural & Molecular Biology* *76*, 145–152.
- Jardetzky, O. (1966). Simple allosteric model for membrane pumps. *Nature* *211*, 969–970.
- Jeschke, G. (2012). DEER Distance Measurements on Proteins. *Annual Review of Physical Chemistry* *63*, 419–446.
- Jin, M.S., Oldham, M.L., Zhang, Q., and Chen, J. (2012). Crystal structure of the multidrug transporter P-glycoprotein from *Caenorhabditis elegans*. *Nature* *490*, 566–569.
- Jin, Y., Nair, A., and Van Veen, H.W. (2014). Multidrug transport protein NorM from *Vibrio cholerae* simultaneously couples to sodium- and proton-motive force. *Journal of Biological Chemistry* *289*, 14624–14632.
- Joosten, R.P., Joosten, K., Murshudov, G.N., and Perrakis, A. (2012). PDB-REDO: Constructive validation, more than just looking for errors. *Acta Crystallographica Section D: Biological Crystallography* *68*, 484–496.
- Kaatz, G.W., Mcaleese, F., and Seo, S.M. (2005). Multidrug Resistance in *Staphylococcus aureus* Due to Overexpression of a Novel Multidrug and Toxin Extrusion ( MATE ) Transport Protein. *Antimicrobiol Agents and Chmotherapy* *49*, 1857–1864.
- Kabsch, W. (2010). XDS. *Acta Crystallographica Section D: Biological Crystallography* *66*, 125–132.
- Karplus, M., and McCammon, J.A. (2002). Molecular dynamics simulations of biomolecules. *Nature Structural Biology* *9*, 646–652.
- Kazmier, K., Sharma, S., Quick, M., Islam, S.M., Roux, B., Weinstein, H., Javitch, J.A., and McHaourab, H.S. (2014). Conformational dynamics of ligand-dependent alternating

- access in LeuT. *Nature Structural & Molecular Biology* *21*, 472–479.
- Korkhov, V.M., and Tate, C.G. (2008). Electron Crystallography Reveals Plasticity within the Drug Binding Site of the Small Multidrug Transporter EmrE. *Journal of Molecular Biology* *377*, 1094–1103.
- Kusakizako, T., Tanaka, Y., Hipolito, C.J., Kuroda, T., Ishitani, R., Suga, H., and Nureki, O. (2016). LCP crystallization and X-ray diffraction analysis of VcmN, a MATE transporter from *Vibrio cholerae*. *Acta Crystallographica Section F Structural Biology Communications* *72*, 552–557.
- Li, L., He, Z., Pandey, G.K., Tsuchiya, T., and Luan, S. (2002). Functional cloning and characterization of a plant efflux carrier for multidrug and heavy metal detoxification. *Journal of Biological Chemistry* *277*, 5360–5368.
- Locher, K.P. (2016). Mechanistic diversity in ATP-binding cassette (ABC) transporters. *Nature Structural & Molecular Biology* *23*, 487–493.
- Lovell, S.C., Davis, I.W., Adrendall, W.B., de Bakker, P.I.W., Word, J.M., Prisant, M.G., Richardson, J.S., and Richardson, D.C. (2003). Structure validation by C alpha geometry: phi, psi and C beta deviation. *Proteins-Structure Function and Genetics* *50*, 437–450.
- Lu, M., Symersky, J., Radchenko, M., Koide, A., Guo, Y., Nie, R., and Koide, S. (2013a). Structures of a Na<sup>+</sup>-coupled, substrate-bound MATE multidrug transporter. *Proceedings of the National Academy of Sciences* *110*, 2099–2104.
- Lu, M., Radchenko, M., Symersky, J., Nie, R., and Guo, Y. (2013b). Structural insights into H<sup>+</sup>-coupled multidrug extrusion by a MATE transporter. *Nature Structural & Molecular Biology* *20*, 1310–1317.
- Marks, D.S., Colwell, L.J., Sheridan, R., Hopf, T.A., Pagnani, A., Zecchina, R., and Sander, C. (2011). Protein 3D structure computed from evolutionary sequence variation. *PLoS ONE* *6*, e28766.
- Martens, C., Stein, R.A., Masureel, M., Roth, A., Mishra, S., Dawaliby, R., Konijnenberg, A., Sobott, F., Govaerts, C., and Mchaourab, H.S. (2016). Lipids modulate the conformational dynamics of a secondary multidrug transporter. *Nature Structural & Molecular Biology* *23*, 744–751.
- Masuda, S., Terada, T., Yonezawa, A., Tanihara, Y., Kishimoto, K., Katsura, T., Ogawa, O., and Inui, K. (2006). Identification and Functional Characterization of a New Human Kidney-Specific H<sup>+</sup>/Organic Cation Antiporter, Kidney-Specific Multidrug and Toxin Extrusion 2. *Journal of the American Society of Nephrology* *17*, 2127–2135.
- Masureel, M., Martens, C., Stein, R. a, Mishra, S., Ruyschaert, J.-M., Mchaourab, H.S., and Govaerts, C. (2014). Protonation drives the conformational switch in the multidrug transporter LmrP. *Nature Chemical Biology* *10*, 149–155.

- McAleese, F., Petersen, P., Ruzin, A., Dunman, P.M., Murphy, E., Projan, S.J., and Bradford, P.A. (2005). A novel MATE family efflux pump contributes to the reduced susceptibility of laboratory-derived *Staphylococcus aureus* mutants to tigecycline. *Antimicrobial Agents and Chemotherapy* *49*, 1865–1871.
- McCoy, A.J., Grosse-Kunstleve, R.W., Adams, P.D., Winn, M.D., Storoni, L.C., and Read, R.J. (2007). Phaser crystallographic software. *Journal of Applied Crystallography* *40*, 658–674.
- Mchaourab, H.S., Steed, P.R., and Kazmier, K. (2011). Toward the fourth dimension of membrane protein structure: Insight into dynamics from spin-labeling EPR spectroscopy. *Structure* *19*, 1549–1561.
- Mishra, S., Verhalen, B., Stein, R.A., Wen, P.C., Tajkhorshid, E., and Mchaourab, H.S. (2014). Conformational dynamics of the nucleotide binding domains and the power stroke of a heterodimeric ABC transporter. *eLife* *2014*, e02740.
- Miwanda, B., Moore, S., Muyembe, J., Nguéfack-tsague, G., Kabangwa, I.K., Ndjakani, D.Y., Mutreja, A., Thomson, N., Thefenne, H., Garnotel, E., et al. (2015). Antimicrobial Drug Resistance of *Vibrio cholerae*, Democratic Republic of the Congo. *Emerging Infectious Diseases* *21*, 847–851.
- Morita, Y., Kodama, K., Shiota, S., Mine, T., Kataoka, A., Mizushima, T., and Tsuchiya, T. (1998). NorM, a Putative Multidrug Efflux Protein, of *Vibrio parahaemolyticus* and Its Homolog in *Escherichia coli*. *Antimicrobial Agents and Chemotherapy* *42*, 1778–1782.
- Morita, Y., Kataoka, A., Shiota, S., Mizushima, T., and Tsuchiya, T. (2000). NorM of *Vibrio parahaemolyticus* Is an Na<sup>+</sup>-Driven Multidrug Efflux Pump. *Journal of Bacteriology* *182*, 6694–6697.
- Morrison, E. a., DeKoster, G.T., Dutta, S., Vafabakhsh, R., Clarkson, M.W., Bahl, A., Kern, D., Ha, T., and Henzler-Wildman, K. a. (2011). Antiparallel EmrE exports drugs by exchanging between asymmetric structures. *Nature* *481*, 45–50.
- Mousa, J.J., Yang, Y., Tomkovich, S., Shima, A., Newsome, R.C., Tripathi, P., Oswald, E., Bruner, S.D., and Jobin, C. (2016). MATE transport of the *E. coli*-derived genotoxin colibactin. *Nature Microbiology* *1*, 15009.
- Murakami, S., Nakashima, R., Yamashita, E., Matsumoto, T., and Yamaguchi, A. (2006). Crystal structures of a multidrug transporter reveal a functionally rotating mechanism. *Nature* *443*, 173–179.
- Nara, T., Kouyama, T., Kurata, Y., Kikukawa, T., Miyauchi, S., and Kamo, N. (2007). Antiparallel membrane topology of a homo-dimeric multidrug transporter, EmrE. *Journal of Biochemistry* *142*, 621–625.
- Nasie, I., Steiner-Mordoch, S., Gold, A., and Schuldiner, S. (2010). Topologically random

- insertion of EmrE supports a pathway for evolution of inverted repeats in ion-coupled transporters. *Journal of Biological Chemistry* 285, 15234–15244.
- Nishima, W., Mizukami, W., Tanaka, Y., Ishitani, R., Nureki, O., and Sugita, Y. (2016). Mechanisms for Two-Step Proton Transfer Reactions in the Outward-Facing Form of MATE Transporter. *Biophysical Journal* 110, 1346–1354.
- Olsson, M.H.M., Søndergaard, C.R., Rostkowski, M., and Jensen, J.H. (2011). PROPKA3: Consistent Treatment of Internal and Surface Residues in Empirical pKa Predictions. *Journal of Chemical Theory and Computation* 7, 525–537.
- Omote, H., Hiasa, M., Matsumoto, T., Otsuka, M., and Moriyama, Y. (2006). The MATE proteins as fundamental transporters of metabolic and xenobiotic organic cations. *Trends in Pharmacological Sciences* 27, 587–593.
- Otsuka, M., Matsumoto, T., Morimoto, R., Arioka, S., Omote, H., and Moriyama, Y. (2005). A human transporter protein that mediates the final excretion step for toxic organic cations. *Proceedings of the National Academy of Sciences of the United States of America* 102, 17923–17928.
- Perez, C., Gerber, S., Boilevin, J., Bucher, M., Darbre, T., Aebi, M., Reymond, J.-L., and Locher, K.P. (2015). Structure and mechanism of an active lipid-linked oligosaccharide flippase. *Nature* 524, 433–438.
- Pos, K.M. (2009). Drug transport mechanism of the AcrB efflux pump. *Biochimica et Biophysica Acta* 1794, 782–793.
- Radchenko, M., Symersky, J., Nie, R., and Lu, M. (2015). Structural basis for the blockade of MATE multidrug efflux pumps. *Nature Communications* 6, 7995.
- Rapp, M., and Granseth, E. (2007). Evolution by Rational Design. *Science* 315, 1282–1284.
- Read, R.J., Adams, P.D., Arendall, W.B., Brunger, A.T., Emsley, P., Joosten, R.P., Kleywegt, G.J., Krissinel, E.B., Lütteke, T., Otwinowski, Z., et al. (2011). A new generation of crystallographic validation tools for the Protein Data Bank. *Structure* 19, 1395–1412.
- Rees, D.C., Johnson, E., and Lewinson, O. (2009). ABC transporters: the power to change. *Nature Reviews Molecular Cell Biology* 10, 218–227.
- Robert, X., and Gouet, P. (2014). Deciphering key features in protein structures with the new ENDscript server. *Nucleic Acids Research* 42, 320–324.
- Seeger, M.A. (2006). Structural Asymmetry of AcrB Trimer Suggests a Peristaltic Pump Mechanism. *Science* 313, 1295–1298.
- Shi, Y. (2013). Common Folds and Transport Mechanisms of Secondary Active Transporters. *Annual Review of Biophysics* 42, 51–72.
- Sjölund-Karlsson, M., Reimer, A., Folster, J.P., Walker, M., Dahourou, G.A., Batra, D.G., Martin, I., Joyce, K., Parsons, M.B., Boncy, J., et al. (2011). Drug-Resistance Mechanisms in

- Vibrio Cholerae O1 outbreak strain, Haiti, 2010. *Emerging Infectious Diseases* 17, 2151–2154.
- Smirnova, I., Kasho, V., Sugihara, J., and Kaback, H.R. (2009). Probing of the rates of alternating access in LacY with Trp fluorescence. *Proceedings of the National Academy of Sciences of the United States of America* 106, 21561–21566.
- Solcan, N., Kwok, J., Fowler, P.W., Cameron, A.D., Drew, D., Iwata, S., and Newstead, S. (2012). Alternating access mechanism in the POT family of oligopeptide transporters. *The EMBO Journal* 31, 3411–3421.
- Stein, R.A., Beth, A.H., and Hustedt, E.J. (2015). A straightforward approach to the analysis of double electron-electron resonance data (Elsevier Inc.).
- Tanaka, Y., Hipolito, C.J., Maturana, A.D., Ito, K., Kuroda, T., Higuchi, T., Katoh, T., Kato, H.E., Hattori, M., Kumazaki, K., et al. (2013). Structural basis for the drug extrusion mechanism by a MATE multidrug transporter. *Nature* 496, 247–251.
- Thompson, J.D., Higgins, D.G., and Gibson, T.J. (1994). CLUSTAL W: Improving the Sensitivity of Progressive Multiple Sequence Alignment Through Sequence Weighting, Position-Specific Gap Penalties and Weight Matrix Choice. *Nucleic Acids Research* 22, 4673–4680.
- Unni, S., Huang, Y., Hanson, R.M., Tobias, M., Krishnan, S., Li, W.W., Nielsen, J.E., and Baker, N.A. (2011). Web Servers and Services for Electrostatics Calculations with APBS and PDB2PQR. *Journal of Computational Chemistry* 32, 1488–1491.
- Ward, J.J., Sodhi, J.S., McGuffin, L.J., Buxton, B.F., and Jones, D.T. (2004). Prediction and Functional Analysis of Native Disorder in Proteins from the Three Kingdoms of Life. *Journal of Molecular Biology* 337, 635–645.
- Waterman, D.G., Winterb, G., Parkhurst, J.M., Fuentes-Monterob, L., Hattne, J., Brewster, A., Sauter, N.K., and Evans, G. (2013). The DIALS framework for integration software. *Ccp4 Newsletter on Protein Crystallography* 16–19.
- Yan, N. (2015). Structural Biology of the Major Facilitator Superfamily Transporters. *Annual Review of Biophysics* 44, 257–283.
- Yin, Y., He, X., Szewczyk, P., Nguyen, T., and Chang, G. (2006). Structure of the multidrug transporter EmrD from Escherichia coli. *Science (New York, N.Y.)* 312, 741–744.

## Original papers

1) Kusakizako, T., Tanaka, Y., Hipolito, C.J., Kuroda, T., Ishitani, R., Suga, H., Nureki, O. (2016).

LCP crystallization and X-ray diffraction analysis of VcmN, a MATE transporter from *Vibrio cholerae*. *Acta Crystallogr. Sect. F Struct. Biol. Commun.* 72, 552–557.

2) Tanaka, Y., Sugano, Y., Takemoto, M., Mori, T., Furukawa, A., Kusakizako, T., Kumazaki, K.,

Kashima, A., Ishitani, R., Sugita, Y., Nureki, O., Tsukazaki, T. (2015). Crystal Structures of SecYEG in Lipidic Cubic Phase Elucidate a Precise Resting and a Peptide-Bound State. *Cell Rep.*

13, 1561–1568.

## Acknowledgements

First, the author would like to thank Professor Osamu Nureki for his supervision and encouragement during the bachelor's, master's and Ph.D. courses. Besides Prof. Nureki, the author has been assisted by many members of the Nureki laboratory. In particular, the author would like to thank Dr. Ryuichiro Ishitani for guidance and assistance with performing experiments and writing papers. The author also would like to thank Dr. Tomohiro Nishizawa, Dr. Hiroshi Nishimasu, Dr. Takanori Nakane, Dr. Tomoya Tsukazaki, Dr. Motoyuki Hattori, and Dr. Ryohei Ishii for technical advice and experimental support, and Ms. Rieko Yamazaki for secretarial assistance.

This study was performed in collaboration with many scientists. The author would like to thank Dr. Hassane S. Mchaourab and Dr. Derek P. Claxton (Vanderbilt University) for the collaboration with the DEER spectroscopic analysis, Dr. Teruo Kuroda (Hiroshima University) for providing the VcmN gene, and Dr. Hiroaki Suga and Dr. Christopher J. Hipolito for providing macrocyclic peptides. The author would also like to thank Dr. Kunio Hirata and Dr. Keitaro Yamashita (SPring-8, BL32XU) for technical support with data collection.

During the bachelor's, master's and Ph.D. courses, the author enjoyed many exciting experiences with the members of the Nureki laboratory. The author thanks Dr. Yoshiki Tanaka, Dr. Takashi Higuchi, Dr. Michio Koyama, Dr. Hideaki Kato, Dr. Kan Kobayashi, Dr. Hironori Takeda, Dr. Shintaro Doki, Dr. Kazuki Kato, Dr. Kaoru Kumazaki, Dr. Naoki Matsumoto, and Mr. Toshiki Kishimoto for stimulating discussions. In particular, the author thanks Mr. Masahiro Fukuda as a supportive labmate since the undergraduate course.

Finally, the author would like to thank his family for continuous support throughout his primary education, the bachelor's, master's and Ph.D. courses, and his life.

Tsukasa Kusakizako